Harmonic Imaging of Nano-confined Aqueous Phase Transitions and the Electrochemical Reduction of Carbon Dioxide Using a Nano-structured Electrolyte

BY

FRANCISCO SCHUNK

B.S., SAINT JOSEPH'S UNIVERSITY, 2016

Advisor: Prof. Christoph G. Rose-Petruck

A DISSERTATION SUBMITTED IN PARTIAL FULFILLMENT OF THE REQUIREMENTS FOR THE DEGREE OF DOCTOR OF PHILOSOPHY IN THE DEPARTMENT OF CHEMISTRY AT BROWN UNIVERSITY

PROVIDENCE, RHODE ISLAND

MAY 2016

This dissertation by Francisco Schunk is accepted in its present form
by the Department of Chemistry as satisfying the
dissertation requirement for the degree of Doctor of Philosophy

Date_____ _____

Christoph G. Rose-Petruck, Advisor

Recommended to the Graduate Council

Date_____ _____

Gerald J. Diebold, Reader

Date_____ _____

Jimmie D. Doll, Reader

Approved by the Graduate Council

Date_____ _____

Peter Weber, Dean of the Graduate School

VITA

Francisco M. Schunk was born on July 28, 1988 in Bethlehem, Pennsylvania. He graduated from Kutztown Area High School in 2007, and matriculated to Saint Joseph's University in Philadelphia that fall. While enrolled at Saint Joseph's University Francisco participated in the Summer Scholars program, conducting research under Dr. John G. Berberian. The Berberian laboratory used 3-bromopentane as a model system to study the supercooled liquid and glassy states of matter via impedance spectroscopy and modulated differential scanning calorimetry. In May 2011 Francisco graduated with a Bachelor of Science in chemistry, and enrolled in the chemistry graduate program at Brown University. While at Brown he conducted his doctoral research under Dr. Christoph Rose-Petruck. Aside from research Francisco also acted as a teaching assistant for several different undergraduate chemistry courses and worked with Dr. Li-Qiong Wang on the development of a novel undergraduate chemistry laboratory.

ACKNOWLEDGEMENTS

There are many people that I must thank for their help and guidance in the completion of my Ph.D., and I am pleased to admit that the majority of these individuals have also become good friends over the time we have spent together. I would like to start by thanking Dr. Christoph Rose-Petruck. As an advisor he obviously guided my graduate career, but the opportunity to learn by watching him work in the laboratory was invaluable. Dr. Rose-Petruck's intuition and creativity were inspiring. I would also like to thank Dr. Gerald Diebold. Besides for teaching graduate thermodynamics Dr. Diebold gave me lessons is glass blowing with a methane torch. The ability to make custom glassware has been a great help in the design of experiments and the ability to quickly test hypotheses.

The Rose-Petruck group members were a fantastic resource to draw from. Yishuo Jiao entered the Rose-Petruck group the same year I did. In traversing graduate school together Yishuo and I grew as scientists and became good friends. Our frequent and free exchange of ideas was stimulating and certainly facilitated the progression of my research. Over many cups of coffee and baskets of chicken wings we shared our perspectives on science, the humanities, our cultures and goals for our time beyond graduate school.

Prior to her graduation from our group Dr. Danielle Rand collaborated with me on a portion of the work presented in this thesis. Dr. Rand along with another former group member Dr. Yanan Liu were responsible for my initial training in the scatter X-ray imaging

technique that became the mainstay of my graduate work. I am grateful to both Dr. Rand and Dr. Liu for their patience and advice.

Daniel DeCiccio is a former Rose-Petruck group member with whom I collaborated on the electrochemical work presented in this thesis. He disseminated the knowledge he gained from literature and trained me in the various experimental techniques used in collecting the relevant data. Daniel's fervor for science and modern technology were a refreshing reminder of the role science plays in our daily lives.

Alexandra Lee and Hongxia Hao joined our research group in the spring of 2015. The opportunity to see the graduate program through their perspectives served as a reminder of lessons learned and since forgotten, which bestowed on me an appreciation for my own experiences that I may not have gained otherwise. For this I am grateful to both of these young ladies.

Dr. Petr Bruza who studied at the Czech Technical University in Prague is one of the most talented experimentalist with whom I have had the pleasure to come in contact with. The time that I spent with Petr while he helped to develop and characterize a plasma X-ray source in our lab was not only educational but most enjoyable. I need to thank Petr for his patience in discussing many experimental techniques with me as well as permitting me to watch him work in the laboratory.

The entire chemistry department made 324 Brook Street my home for five years and to not thank them would be a grave error. Sheila Quigley and Rose Barreira in the main office ensured that I did everything necessary to remain in good standing within the graduate program. Alan Sylvia, Rob Wilson and Eric Friedfeld in the stockroom enabled

the purchasing of all the laboratory equipment that I accumulated over my time at Brown. Ken Talbot and Randy Goulet machined many costume pieces without which there would have been little to no progress made in my research. Al Tente the department electrician resolved any issues I came across with the electronic components of my experiments. Carol DeFeciani and Margaret Doll are also owed my thanks for their technical support with all things computer related.

I must thank my family for their love and support throughout this process. My mother and father Marta and James Schunk made all of my success possible. My sister Simone has been a motivating inspiration since a young age, and while attending school in Philadelphia Simone and her husband Jeremy Mock opened their home to me so I might briefly escape college life for a few hours of sanity. It goes without saying that my twin brother James has had a profound effect on my life and without whom I would not be the person I am today.

The last person that I must thank is Kathryn Voelkner, my girlfriend of over 5 years. We lived together for most of my graduate career, so she would see firsthand the late nights and early mornings I spent working both at home and in the laboratory. Amidst moments of great stress and self-doubt Kathryn would offer kind words and always made me laugh.

CONTENTS

List of Tables

List of Figures

Chapter 1 Introduction

1.1 Motivation

As of late nanoscience has been the recipient of ever-increasing interest and resources from the scientific community, however it is by no means a new discipline. By adding powders of metal oxide nanoparticles to glass melts the ancients took advantage of the particles' surface plasmon resonances to produce brilliantly colored glass pieces. Equipped with the theoretical and experimental arsenal of modern science we have gained a greater appreciation of the potential nanomaterials hold for revolutionizing medicine and engineering. In order to unlock the potential of mesoscale objects it is paramount that we obtain a level of understanding of their properties and an ability to manipulate matter on this size scale that has not yet been achieved.

The advent of electron microscopy and scanning probe microscopy facilitated the characterization of nanomaterials by circumventing the diffraction limited resolution of optical imaging systems and providing a means of manipulating matter at the mesoscale. Examples of these techniques are transmission electron microscopy (TEM), scanning electron microscopy (SEM) and atomic force microscopy (AFM). Small angle X-ray scattering (SAXS) is a more mature method of studying nanometer sized objects, yielding information about particle size, shape and orientation. The previously mentioned experimental procedures all probe relatively small sample sizes and are well suited for the characterization of nanoscale entities in vacuo. By virtue of the sample sizes probed these

techniques all suffer from the same limited capability in studying heterogeneous samples or offering a measure of the significance of a particle's incorporation into a complex environment.

TEM, SEM and AFM may only make observation of at most several nanoparticles. TEM and SEM suffer from the added limitation of requiring a high vacuum environment for the propagation of an electron beam. The cross-section area of an X-ray beam used for SAXS probes a much larger sample area than TEM, SEM or AFM but by no means constitutes what would generally be considered as a large viewing field. The limitations of these techniques prohibits the observation of large numbers of nanoparticles in an extended environment without the expense of conducting raster scans. For the sake of being concrete consider the examples of nanoparticle contrast agents injected into a large multicellular organism and a nano-structured battery electrode. The distribution of nanoparticles in the multicellular organism improve contrast in an image and may additionally indicate the presence of a foreign body. The distribution of nanoparticles in the battery as well as changes to their properties is an indication of electrode aging. In these examples it is not only the properties of the particles themselves that is of interest, but also how the particles interact with their environment as a whole. A large viewing field methodology is necessary to capture a measure of such an interaction through the observation of inhomogeneities formed over length scales that are large compared to the particle size.

The work presented in this thesis primarily involves the application of an X-ray scatter imaging technique, termed X-ray Spatial Frequency Heterodyne Imaging (SFHI), which utilizes a large viewing field. SFHI was used to observe liquid water confined to the inner cavity of multi-walled carbon nanotubes (MWCNTs). Both wet carbon nanotube

(CNT) samples and dry reference samples were imaged simultaneously, so the inhomogeneity in this case can be considered as the difference between the wet and dry samples which were arranged over a macroscopic distance. The data collected constitutes the first set of experimental evidence that the behavior of liquid water confined to spaces of less than 10 nm is predictable by equilibrium thermodynamics.

A second work presented in this thesis made utilization of clathrate hydrates as an electrolyte in the electrochemical reduction of carbon dioxide to more chemically versatile species. Clathrate hydrates are nano-sized crystallites of water molecules that may be occupied by a guest molecule, in this case carbon dioxide. Loading of clathrate cages increased the carbon dioxide concentration in solution which promoted the production of heavier hydrocarbons, increased the Faraday efficiency for the production of carbonaceous products at low over potentials and suppressed the hydrogen evolution reaction relative to similar experiments devoid of clathrates.

1.2 Capillary Theory, Nanofluidics and Water filled CNTs

1.2.1 Introduction

Liquids confined to spaces with dimensions on the nanoscale exhibit properties that differ from those of bulk liquids[1-4]. The deviation of nano-confined liquid properties from those of bulk liquids remains one of the lesser explored components of the nanoscience landscape[5]. Dependence of liquid properties on confinement is by itself not a surprising notion. From surface chemistry and physics it is known that the physical properties of liquids vary continuously, typically over the nanometer scale, as an interface is approached

from within the bulk[6-7]. Thus when liquids are confined to nanometer size confinements surface-liquid interaction can come to dominate liquid-liquid interaction. A common example of liquid properties dictated by confinement is capillary condensation. Small pores promote condensation permitting a liquid and its vapor to coexist below the saturation pressure. The behavior of liquids confined to nanoscale spaces finds application in the fields of transmembrane transport[8], transport and sequestration of gasses and liquids in porous minerals[9], chromatography[10], purification and chemistry[11].

Liquid water and carbon nanotubes is a favored system in the study of nanofluidics amongst both the experimental and theoretical camps. A seminal work of nanofluidics involving carbon nanotubes (CNTs) was carried out by Dujardin et. al.,[12] in which they concluded that liquids with interfacial tensions of less than 200 millinewtons per meter will wet and capillary fill MWCNTs with inner diameters between 5 and 10 nm. The conclusion was reached through a systematic introduction of different elemental liquids of known surface tension into MWCNT powders. After solidification of the liquid phases, wetting was observed via TEM. In finding the threshold surface tension above which liquids do not wet CNTs it was demonstrated that liquid water with a surface tension of 72 mN/m wets and fills CNTs despite their insolubility in water.

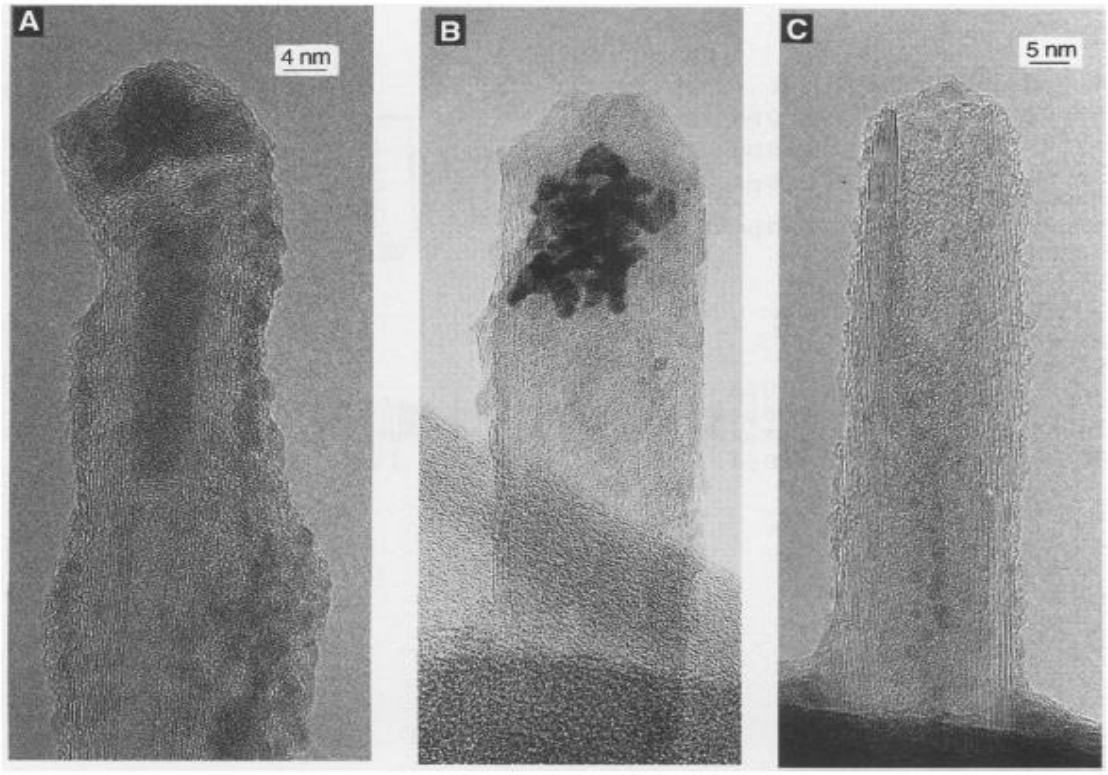

Figure 1.1 MWCNTs that have been capillary filled by selenium (A) and cesium (B and C)[12]. In Figure C faint cesium particles can be seen near the bottom of the image within the CNT. Elemental powders were heated past their melting points and then exposed to the CNTs. The samples were cooled and then imaged via TEM. Only the occupation of the inner CNT pores by a solid could be imaged. The high vacuum of a TEM would cause any liquid to evaporate.

1.2.2 Capillary Theory

Wetting and capillary filling phenomena may be addressed to a cursory degree by the Young-Laplace and Kelvin equations. The pressure difference between a liquid and gas in terms of the curvature of the meniscus interface is given by the Young-Laplace equation. The Young-Laplace equation is written

$$\Delta P = \gamma\left(\frac{1}{R_1} + \frac{1}{R_2}\right), \qquad 1.1$$

where $\Delta P = P_l - P_g$ is the pressure difference between the liquid and gas phases, γ is the surface tension of the liquid and R_1 and R_2 are the principle radii of curvature of the interface. ΔP is often referred to as the Laplace pressure. The radii of curvature are taken to be positive if the center of curvature lies within the liquid. In other words the pressure is always higher on the convex side of the meniscus. The term gas and not vapor is used above because the Young-Laplace equation is not substance specific. It is derived from mechanical equilibrium considerations, so the liquid and gas may be composed of different species.

If applied to capillary condensation within a capillary of circular cross-section the Young-Laplace equation becomes

$$\Delta P = \frac{2\gamma cos\theta}{r}, \qquad 1.2$$

by first recognizing that a hemispherical meniscus will form in such a capillary making the radii of curvature equal, $\left(\frac{1}{R_1} + \frac{1}{R_2}\right) = \frac{2}{R}$. Then upon the substitution $R = \frac{r}{cos\theta}$ where r is the radius of the capillary cross-section and θ is the contact angle between the liquid and capillary, equation 1.2 is obtained. In the case of capillary filling the liquid must wet the capillary meaning the contact angle must be acute, yielding a negative Laplace pressure. A negative Laplace pressure means that the pressure inside of the liquid phase is less than that of the gas phase with which it is in contact.

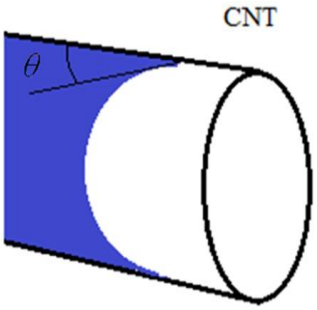

Figure 1.2 Illustration of water confined to the inner cavity of a CNT. The contact angle between the liquid-gas interface and the liquid-solid interface is labeled by the Greek letter theta. In the figure the contact angle is acute and the radii of curvature is negative demonstrating that water wets the CNT inner surface.

The Kelvin equation addresses the change in vapor pressure of a liquid with curvature of the liquid-vapor interface. The Laplace pressure is the cause for the variation of vapor pressure with the curvature of the liquid surface. The change in molar Gibbs energy in going from a planar to a curved surface geometry may be found by integration of the molar Gibbs energy with respect to pressure at constant temperature. This integration yields the Young-Laplace equation again within a multiplicative factor equal to the molar volume of the liquid

$$\Delta g = \int_0^{\Delta P} v dP = v\Delta P = v\gamma \left(\frac{1}{R_1} + \frac{1}{R_2}\right). \qquad 1.3$$

Above Δg is the change in molar Gibbs free energy, ΔP is the Laplace pressure and v is the molar volume of the liquid. The change in Gibbs energy for the vapor goes as

$$\Delta g = RTln\left(\frac{P}{P_o}\right), \qquad 1.4$$

where R is the gas constant, T the temperature in Kelvin, P_o is the vapor pressure above a planar interfacial geometry and P is the vapor pressure above a curved interfacial geometry.

If the liquid and its vapor are to remain in equilibrium equations 1.3 and 1.4 must be equal, giving the Kelvin equation

$$RTln\left(\frac{P}{P_o}\right) = v\gamma(\frac{1}{R_1} + \frac{1}{R_2}). \quad 1.5$$

Under the same sign convention used for the Young-Laplace equation the radii of curvature is negative for a liquid that wets the inside of a capillary, resulting in a decrease in vapor pressure relative to that of a planar interfacial geometry. An immediate consequence of the decrease in vapor pressure for a liquid inside of a capillary is an increase in boiling point temperature.

An estimate for the change in boiling point of a liquid due to capillary confinement can be gotten from a combination of the Kelvin and Clausius-Clapeyron equations. The Clausius-Clapeyron equation determines the coexistence curve for two phases of a substance in the P-T plane and is expressed

$$ln\left(\frac{P_f}{P_i}\right) = \frac{\Delta H_{vap}}{R}(\frac{1}{T_i} - \frac{1}{T_f}). \quad 1.6$$

The corresponding pressures and temperatures along the coexistence curve are labeled accordingly, ΔH_{vap} is the molar enthalpy of vaporization and R is the gas constant. The enthalpy of vaporization is used because in the current discussion we are considering a liquid in equilibrium with its vapor. For the case of a circular cross-section capillary and zero contact angle the Kelvin equation is

$$RT_i ln\left(\frac{P}{P_o}\right) = \frac{2v\gamma}{r}, \quad 1.7$$

and upon substitution of equation 1.6 into equation 1.7

$$RT_i \frac{\Delta H_{vap}}{R}\left(\frac{1}{T_i}-\frac{1}{T_f}\right)=\frac{2v\gamma}{r}. \quad 1.8$$

In equation 1.7 the temperature at which the deformation of the interface is to take place is the boiling point of the liquid with a planar interfacial geometry under pressure P_o, and has been re-labeled T_i in anticipation of its equivalence with the initial temperature in the Clausius-Clapeyron equation. Also P_o and P in the Kelvin equation have been equated with P_i and P_f respectively from the Clausius-Clapeyron equation. Solving for T_f

$$T_f = \frac{T_i}{1-\frac{2v\gamma}{\Delta H_{vap} r}}. \quad 1.9$$

Using values for water T_i is taken as 373 K, v has the value 1.8x10^{-5} m^3/mol, γ is equal to 58.85x10^{-3} N/m, ΔH_{vap} is 40.65x10^3 J/mol and assigning the capillary radius r as 0.5x10^{-9} m the boiling point for liquid water confined to a capillary of diameter 1 nm under atmospheric conditions is found to be approximately 416 K. A 43 degree increase in boiling point due to confinement would permit chemical reactions in water to proceed with elevated kinetics that could not be otherwise achieved without increased pressure. In section 1.2.4 evidence from literature will show that it is inappropriate to speak of the boiling point of water in its common context when the water is confined to spaces of less than 3 nm.

1.2.3 Liquids Confined to Large Diameter CNTs

The experimental work found in literature on the behavior of water confined to CNTs is generally restricted two classes of CNT diameter, greater than 70 nm and less than 3 nm. Two experimental studies to take note of from the larger regime of CNT diameters made observation of the behavior of liquids confined to MWCNTs with diameters of

approximately 150 nm and 70 nm. Rossi et. al.[13] used Environmental Scanning Electron Microscopy (ESEM) to observed condensation of water into MWCNTs with inner diameters as small as 150 nm. They reported the formation of thin films of water propagating along the CNT walls. Upon further condensation the thin films collapsed to form a lens shaped meniscus that grew outwards until forming a flat meniscus at the CNT open ends. Changes in the CNT cross-section geometry were also observed to accompany the different stages of filling. A uniform radial contraction was associated with the formation of thin films on the CNT inner walls, the cross-section took the shape of an ellipse upon the formation of a lens shaped meniscus and finally the CNTs regained their original cross-section geometry once filling was complete. The change in CNT cross-section geometry was attributed to the disjoining pressure within the confined liquid phase. The disjoining pressure is an additional force per unit area produced by the proximity of two interfaces in a thin film that make the hydrostatic pressure within the film different than that of the bulk liquid[14].

The specific manner in which water condenses into a rigid cylindrical capillary was proposed by Everette and Haynes[15]. Expressing the effective surface area and volume of the condensate in terms of the liquid surface mean curvature and using the conditions of mechanical and thermal equilibrium as constraints on these expressions, it was demonstrated that condensation forms an unduloidal liquid surface, followed by a lens shaped meniscus that subsequently propagates toward the capillary ends. This series of condensate configurations predicted by thermodynamics is the same as that observed for condensation of water into MWCNTs of 150 nm inner diameter, confirming that liquids confined to spaces of this size have behavior governed by thermodynamic equations.

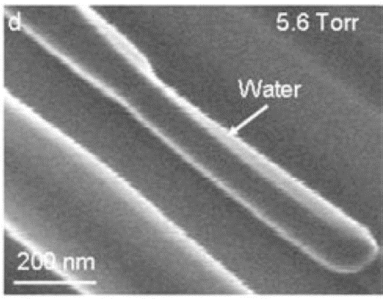

Figure 1.3 ESEM of liquid water thin film formation on the inner surface of a MWCNT accompanied by a contraction of the CNT cross-section geometry[13].

Yazicioglu et. al.[16] used the electron beam of a TEM to simultaneously locally heat and image fluid confined to MWCNTs with diameters of 70 nm. They observed the formation of liquid-vapor interfaces with negative radii of curvature suggesting that the applicability of equilibrium thermodynamics to confined liquids may be extended from confinements of 150 nm down to 70 nm.

a. **b.**

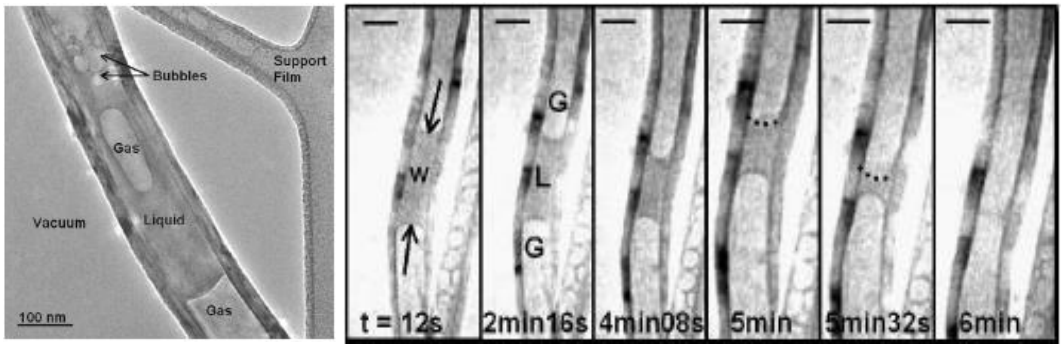

Figure 1.4 In Figure **a.** an electron beam was used to locally heat liquid confined to the inner pore of a MWCNT. Figure **b.** shows a series of TEM images taken in time as liquid confined to CNTs was heated by a resistive heating stage at a rate of 40 degrees per minute. The liquid completely evaporated at 260 ^{o}C. The scale bar is 100 nm[16].

1.2.4 Liquids Confined to Small Diameter CNTs

The two studies mentioned in section 1.2.3 are exceptional in the size of CNTs used. The majority of activity in nanofluidics research utilizing CNTs makes use of single-walled carbon nanotubes (SWCNTs) with inner diameters less than 3 nm, a length which corresponds to approximately 10 water molecules. From various sources in literature it has been generally found that water confined to SWCNTs with inner diameters of less than 3 nm has behavior that is strikingly different from that of bulk water in that highly ordered structures form along the tube axis. The ordered water structures have come to be widely labeled as nanotube water. The presence of water confined to small diameter SWCNTs and its ordering has been observed by X-ray diffraction (XRD)[17-19], NMR[18, 20], adsorption isotherms[20], neutron scattering[21] and molecular dynamics simulations[22-24]. Kyakuno et. al.[18] and Kolesnikov et. al.[21] reported the existence of a nanotube water monolayer with a structure like that of bulk ice just within the SWCNT surface, and a linear chain of water occupying the inner space of the nanotube water configuration. Kolesnikov et. al. further reported that the inner water chain retained fluid like dynamics at temperatures as low as 50 K. Kyakuno et. al. reported wet-dry transitions at low temperatures, which were dependent upon CNT diameter. Maniwa[17] and Kyakuno observed reversible evacuation and re-occupation of water out of and back into SWCNTs upon heating and cooling.

A molecular dynamics study conducted by Thomas et. al.[24] demonstrated that water density inside and outside of a CNT is highest at the CNT surface and oscillates as it approaches a limit with increasing distance from the CNT surface. Water on the exterior of the CNT was shown to approach a density of bulk water at a distance of 1 nm from the surface. This study is unique in that it is one of the few that simulated CNTs with diameters

as large as 10.4 nm. The diameters included in the simulation were 1.1nm, 2.8 nm, 6.9 nm and 10.4 nm. Water confined to the 1.1 nm diameter tube was seen to form a pentagon structure with density equal to that of the first exterior water layer. The average water density within the 2.8 nm diameter CNT was significantly less than that of bulk water. Water within the 6.9 nm diameter tube had a similar density profile to the unconfined water and the density became equal to that of bulk water at a distance slightly greater than 1 nm from the CNT surface, i.e. confined water removed a sufficient distance from the CNT wall had behavior indistinguishable from bulk water. Water confined to the 10.4 nm diameter nanotube behaves almost identically to the unconfined water and approached the behavior of bulk water at the tube center just as with the simulation involving the 6.9 nm diameter CNT.

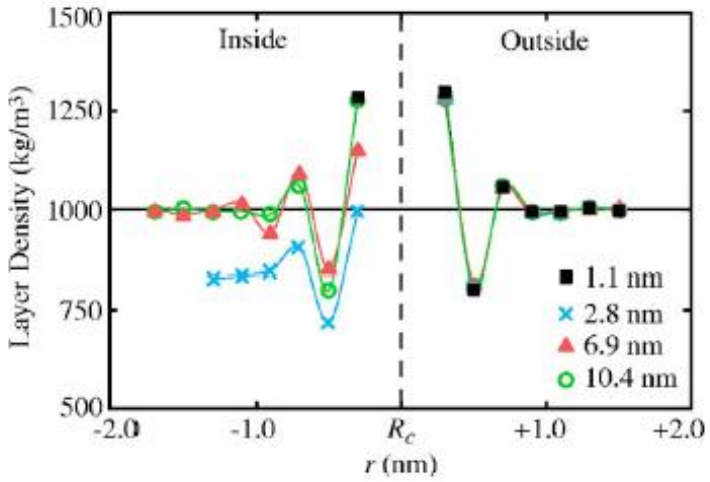

Figure 1.5 Density of liquid water confined to CNTs of different diameters. The density is shown for water on the interior and exterior of the CNTs. For diameters less than 3 nm the density of water is different from that of water on the exterior of the tube. When the diameter is 6.9 nm the density profile is nearly the same as that of the unconfined water, and for a diameter of 10.4 nm the density profiles of confined and unconfined water are identical.[24]

To recapitulate the relevant literature delineated in the preceding sections, it has been shown experimentally that liquid confined to the inner cavity of CNTs with diameters of 70 nm and greater has properties predictable by equilibrium thermodynamics. For CNT with diameters of less than 3 nm confined liquids can no longer be considered as a structureless continuum and their molecular identity is apparent. Therefore the dominion of equilibrium thermodynamic equations over the behavior of confined water terminates somewhere between confinements of sizes 70 nm and 3 nm. The theoretical work conducted by Thomas et. al.[24] predicted that the equilibrium thermodynamic description of confined water breaks down below confinements of 6.4 nm, effectively narrowing the range established experimentally.

1.3 Electrochemical Reduction of CO_2 Using a Nano-structured Electrolyte and Electrode

1.3.1 Electrochemical Reduction of CO_2

The electrochemical reduction of CO_2 has increasing relevance amidst the backdrop of industrial migration toward renewable energy technologies and the desire to arrive at a viable alternative to fossil fuels. Hori et. al.[25] conducted a systematic study of CO_2 reduction using different metal electrodes. Copper was found to have the best performance as an electrocatalyst for the reduction of CO_2 to higher valued products including methane, formic acid and ethylene. The reaction proceeds at high overpotentials, is non-selective and is accompanied by the competing hydrogen evolution reaction (HER) but copper is still held as the best choice. Historically CO_2 saturated electrolyte solutions are used as a method of delivery to the metal electrodes, but previous studies indicate that the low

solubility of CO_2 in water limits conversion[26-27]. Solubility may be increased with pressure but high pressure systems are expensive and increase experimental complexity. Cooling has a negligible advantage in surmounting the solubility shortcomings of aqueous electrolyte solutions because the amount of solvated CO_2 in water only approximately doubles upon going from 298 K to 273 K[26].

At sufficiently high pressures and low temperatures water containing solvated gasses form inclusion compounds called clathrate hydrates. The gasses occupy and stabilize the host clathrate cages but do not chemically bond[28]. Gasses capable of forming clathrates include CO_2[29-32], CH_4[33-34], N_2[35], CO[36-37], H_2[38] and hydrocarbons[39-40]. The solubility of CO_2 in clathrate hydrates can be up to two orders of magnitude greater than that for liquid water.

Addition of tetrahydrofuran (THF) to water negates the need for solvated gasses and high pressures for clathrate formation, and the density of clathrate crystallites depends on THF concentration[41-43]. For a solution of 1.5 mol% THF, clathrates form at atmospheric pressure and 0 ^oC[42, 44]. THF occupies the larger of the clathrate cages slightly diminishing the clathrate loading capacity with respect to solute gasses[32]. The occupation of clathrate cages by CO_2 is spontaneous and more energetically favorable relative to other gases. As a result CO_2 can be enriched within clathrates relative to a gaseous mixture. Using a 1 mol% THF water solution at 277 K a 50 mol% CO_2 clathrate phase may be produced using a gas mixture of 30 mol% CO_2 and 70 mol% N_2 at 7 bar[45].

Chapter 2 X-ray Diffraction Theory

2.1 Scattering by an Arbitrary Object

2.1.1 The Scattered Amplitude

The arguments below closely follow those presented by Guinier[46] in his text on X-ray diffraction and summarize the necessary information needed to discuss the X-ray imaging methodology and the theoretical interpretation of the data collected through its use. The fundamental theoretical tool of X-ray diffraction is the scattering factor f, which in general is equal to the ratio of the scattered wave amplitude A to the amplitude of the incident wave A_0,

$$f = \frac{A}{A_0}. \tag{2.1}$$

The scattering factor of an electron is given by

$$f = \int \rho(\vec{x}) e^{-i\vec{q}\cdot\vec{x}} dv, \tag{2.2}$$

where $\vec{x}$ is the object space position vector and ρ is the electron density. The electron density is calculated $\rho(\vec{x}) = |\psi(\vec{x})|^2$, and $\psi(\vec{x})$ is the electronic wave function gotten from Schrodinger's equation. The scattering vector $\vec{q}$ is equal to the vector in the direction of the scattered wave $\vec{s}$ minus the vector in the direction of the incident wave $\overrightarrow{s_0}$ times 2π divided by the wavelength of radiation λ

$$\vec{q} = 2\pi \frac{\vec{s} - \vec{s}_0}{\lambda}. \tag{2.3}$$

If the scattering angle is taken as 2θ, then the norm of the scattering vector is

$$|\vec{q}| = \frac{4\pi sin\theta}{\lambda}. \qquad 2.4$$

The scattering vector may also be identified as the angular spatial frequency vector. The integral in equation 2.2 is taken over all of object space. Under the assumption that multi-electron structures like atoms and molecules have total electron densities that can be approximated as the sum of the constituent electron densities, multi-electron scattering factors for such structures can be calculated by summation over the elementary electronic scattering factors. For example if f is a desired scattering factor for a multi-electron atom with atomic number Z it is calculated by

$$f = \sum_{j=1}^{Z} f_j, \qquad 2.5$$

where f_j is the scattering factor for the jth electron

$$f_j = \int \rho_j(\vec{x}) e^{-i\vec{q}\cdot\vec{x}} dv. \qquad 2.6$$

Scattering factors for increasingly complicated objects can be generated by summation over the constituent atomic scattering factors and so on until the desired level of complexity is reached. For more complicated structures an alternative and more direct method of calculating scattering factors is summation over constituent electron density functions to arrive at a collective electron density. For a sample with N atoms whose positions are given by $\{\vec{x}_k\}$ and electron densities $\rho_k(\vec{x} - \vec{x}_k)$ the total electron density of the object is $\rho(\vec{x}) = \sum_{k=1}^{N} \rho_k(\vec{x} - \vec{x}_k)$. The scattering factor for the sample is then

$$f = \int \rho(\vec{x}) e^{-i\vec{q}\cdot\vec{x}} dv. \qquad 2.7$$

2.1.2 The Scattered Intensity

The diffracted amplitude is in general complex and therefore not of particular interest as it does not correspond to a physical quantity. The intensity of the scattered wave is the real valued quantity observed in an experiment and equals the square of the amplitude modulus,

$$I = |A|^2 = A^* A = |f A_0|^2 = |f|^2 I_0. \qquad 2.8$$

The vertical lines denote calculation of the norm or modulus, and the superscript asterisk indicates taking the complex conjugate. The intensity of the incident beam is I_0.

In theoretical calculations of diffraction patterns the unit of measure is often taken as the intensity scattered by a single electron in place of the sample with all other experimental parameters held constant. In the case of coherent scattering this assignment renders the total scattered amplitude equal to the scattering factor and the intensity is then the square of the scattering factor modulus

$$I_N = |f|^2. \qquad 2.9$$

The intensity I_N is labeled the scattering power. Equation 2.9 for the scattering power is not generally useful for data interpretation because the scattering factors depend explicitly on the phase of the diffracted wave

$$\varphi = -\vec{q} \cdot \vec{x}, \qquad 2.10$$

which is not detected. To arrive at a more pragmatic formula for the scattering power of an object substitute the definition of a scattering factor into the expression for the scattering power

$$I_N(\vec{q}) = \int \rho(\vec{u}) e^{i\vec{q}\cdot\vec{u}} dv_u \int \rho(\vec{u}') e^{-i\vec{q}\cdot\vec{u}'} dv_{u'} = \int\int \rho(\vec{u})\rho(\vec{u}') e^{-i\vec{q}\cdot(\vec{u}'-\vec{u})} dv_u dv_{u'}.$$

2.11

Let $\vec{x} = \vec{u}' - \vec{u}$

$$I_N(\vec{q}) = \int\int \rho(\vec{u})\rho(\vec{x}+\vec{u}) e^{-i\vec{q}\cdot\vec{x}} dv_x dv_u = \int \mathcal{P}(\vec{x}) e^{-\vec{q}\cdot\vec{x}} dv_x, \qquad 2.12$$

where

$$\mathcal{P}(\vec{x}) = \int \rho(\vec{u})\rho(\vec{x}+\vec{u}) dv_u. \qquad 2.13$$

Equation 2.13 is called the Patterson function and is the autocorrelation of the object electron density. From equation 2.12 the scattering power of an object is equal to the Fourier transform of its Patterson function. By the Fourier inversion theorem the Patterson function of the object is equal to the inverse Fourier transform of the scattering power

$$\mathcal{P}(\vec{x}) = \int I_N(\vec{q}) e^{i\vec{q}\cdot\vec{x}} dv_q, \qquad 2.14$$

with integration carried out over reciprocal space. The consequence of this expression is that X-ray diffraction experiments result in the calculation of the Patterson function of the object and not the electron density. Structural details about the object beyond what is contained within the Patterson function are unobtainable by diffraction experiments.

In the case that an object is composed of N identical particles the scattering power may be written

$$I_N(\vec{q}) = N|F|^2 \bar{v} \int \frac{\mathcal{P}_a(\vec{x})}{V} e^{-i\vec{q}\cdot\vec{x}} dv_x, \qquad 2.15$$

where

$$\mathcal{P}_a(\vec{x}) = \int \rho_a(\vec{u})\rho_a(\vec{x}+\vec{u})dv_u. \qquad 2.16$$

Equation 2.16 is the particulate Patterson function, ρ_a is the particle density, V is the object volume such that $\bar{v} = \frac{V}{N}$ is the average volume available for each atom or atomic group and F is the scattering factor for one of the N identical particles. Articulating the scattering power in terms of its dependence on the particulate Patterson function will prove useful in the decomposition of the scattering power into terms dependent upon the shape and size of the object and on its internal particulate structure.

2.2 Scattering by a Statistically Homogeneous Object

In most samples the configuration of particles is not precisely fixed, so it is the intensity due to the average configuration that is being measured in a given experiment. The average measured intensity is equal to the Fourier transform of the average Patterson function of the object

$$\bar{I}_N(\vec{q}) = \int \bar{\mathcal{P}}(\vec{x})e^{-\vec{q}\cdot\vec{x}}dv_x = N|F|^2\bar{v}\int \frac{\bar{\mathcal{P}}_a(\vec{x})}{V}e^{-i\vec{q}\cdot\vec{x}}dv_x. \qquad 2.17$$

For a statistically homogeneous object the distribution of atoms or molecules is independent of which particle position is chosen as the origin, and it is possible to decompose the scattering power into terms reliant on the size and shape of the object and its atomic structure by relating the average particulate Patterson function to the statistical distribution of matter. The statistical distribution of matter is

$$z(\vec{x}) = \delta(\vec{x}) + \frac{1}{\bar{v}}p(\vec{x}). \qquad 2.18$$

The first term is the Dirac delta function, $\bar{v}$ is the average volume available for each particle defined previously and $p(\vec{x})$ is the pair distribution function. For objects devoid of long range order the pair distribution function oscillates about unity for $\vec{x}$ near the origin and approaches a limiting value of one with increasing distance from the origin. For such objects the statistical distribution of matter can be expressed by

$$z(\vec{x}) = \delta(\vec{x}) + \frac{1}{v_1} + \frac{1}{v_1}[p(\vec{x}) - 1]. \qquad 2.19$$

The second term is the limiting portion of the pair distribution function and third term is the fluctuating part. The ratio $\frac{\bar{\mathcal{P}}_a}{V}$ is the average value of the particulate Patterson function calculated over an arbitrary volume within the object. For infinite homogeneous matter the ratio is independent of the volume chosen. By partitioning the volume V into small volume elements dv, the integral is equal to the sum of N terms of the form $\rho_a(\vec{u})\rho_a(\vec{u}+\vec{x})dv$ where $\rho_a(\vec{u})dv = 1$. N is the number of particles in the volume V. Only these terms contribute to the calculation of the average particulate Patterson function since $\rho_a(\vec{u})dv = 0$ otherwise. The average value of $\rho_a(\vec{u}+\vec{x})$ is equal to the statistical distribution of matter

$$z(\vec{\xi}) = \overline{\rho_a(\vec{u}+\vec{x})} = \frac{1}{|\vec{\epsilon}|}\int_{\vec{\xi}-\frac{\vec{\epsilon}}{2}}^{\vec{\xi}+\frac{\vec{\epsilon}}{2}} \rho_a(\vec{\xi'})\, dv_{\xi'}, \quad \vec{\xi} = \vec{u}+\vec{x} \quad \text{and} \quad \vec{\xi} \times \vec{\epsilon} = 0, \qquad 2.20$$

for some small interval $|\vec{\epsilon}|$. Then

$$\frac{\bar{\mathcal{P}}_a(\vec{x})}{V} = \frac{N}{V} z(\vec{\xi}) = \frac{z(\vec{\xi})}{\bar{v}}. \qquad 2.21$$

In a statistically homogeneous object the density of matter is independent of choice of origin throughout the object, meaning the external surfaces of the object have no effect on the distribution of matter. The matter density of such an object can be factored into a

translationally invariant density that extends infinitely in all directions $\rho_\infty(\vec{x})$ and the object's form factor $\sigma(\vec{x})$

$$\rho(\vec{x}) = \rho_\infty(\vec{x})\,\sigma(\vec{x}). \qquad 2.22$$

The form factor is equal to one inside of the object volume and zero otherwise. The particulate Patterson function becomes

$$\mathcal{P}_a(\vec{x}) = \int \rho_{a\infty}(\vec{u})\rho_{a\infty}(\vec{u}+\vec{x})\,\sigma(\vec{u})\sigma(\vec{u}+\vec{x})dv_u. \qquad 2.23$$

Let $\mathcal{V}(\vec{x})$ represent the autocorrelation of the object form factor

$$\mathcal{V}(\vec{x}) = \int \sigma(\vec{u})\sigma(\vec{u}+\vec{x})dv_u, \qquad 2.24$$

then

$$\mathcal{P}_a(\vec{x}) = \int_{\mathcal{V}(\vec{x})} \rho_{a\infty}(\vec{u})\rho_{a\infty}(\vec{u}+\vec{x})\,dv_u, \qquad 2.25$$

because only the region of object space where the form factor autocorrelation is different from zero contributes to $\mathcal{P}_a(\vec{x})$. Re-writing equation 2.25,

$$\mathcal{P}_a(\vec{x}) = \overline{\rho_{a\infty}(\vec{u})\rho_{a\infty}(\vec{u}+\vec{x})}\,\mathcal{V}(\vec{x}). \qquad 2.26$$

The average taken in the right hand side was already shown to be equal to the statistical distribution of matter divided by the average volume available to each particle

$$\mathcal{P}_a(\vec{x}) = \frac{z(\vec{x})}{\bar{v}}\mathcal{V}(\vec{x}). \qquad 2.27$$

The assumption of statistical homogeneity was invoked by equating $\rho_{a\infty}(\vec{u}+\vec{x})$ with $\overline{\rho_{a\infty}(\vec{u}+\vec{x})}$ in arriving at equation 2.27. Upon making this substitution into equation 2.17 the scattering power is equal to the Fourier transform of the product $z(\vec{x})\mathcal{V}(\vec{x})$. By the

Fourier autocorrelation theorem the transform of $\mathcal{V}(\vec{x})$ is equal to the modulus squared of the form factor's Fourier transform. If $\Sigma(\vec{q})$ denotes the transform of the form factor $\mathcal{F}\{\sigma(\vec{x})\}$, then $\mathcal{F}\{\mathcal{V}(\vec{x})\} = |\Sigma(\vec{q})|^2$.

The Fourier convolution theorem states that upon transformation to or from reciprocal space a product becomes a convolution, making the scattering power

$$I_N(\vec{q}) = N|F|^2 \int \frac{z(\vec{x})\mathcal{V}(\vec{x})}{V} e^{-i\vec{q}\cdot\vec{x}} dv_x = \frac{N}{V}|F|^2[|\Sigma(\vec{q})|^2 * Z(\vec{q})]. \qquad 2.28$$

The transform of the statistical distribution $z(\vec{x})$ is represented by $Z(\vec{q})$, and the asterisk in the square braces indicates a convolution. Expanding the statistical distribution transform, the scattering power is

$$I_N(\vec{q}) = \frac{N}{V}|F|^2 \left[|\Sigma(\vec{q})|^2 * \frac{\delta(\vec{q})}{\bar{v}} + |\Sigma(\vec{q})|^2 * \Phi(\vec{q})\right], \qquad 2.29$$

where

$$\Phi(\vec{q}) = 1 + \frac{1}{\bar{v}}\int [p(\vec{x}) - 1] e^{-i\vec{q}\cdot\vec{x}} dv_x. \qquad 2.30$$

The autocorrelation of the form factor is centrosymmetric with a global maxima at the origin. The Fourier transform of a centrosymmetric function is again centrosymmetric[47]. Therefore, $|\Sigma(\vec{q})|^2$ is a centrosymmetric peak with a global maxima at the origin and a width approximately equal to V^{-3}. Given these properties $|\Sigma(\vec{q})|^2$ is in general a sharp peak about the origin of reciprocal space that only becomes observable for submicroscopic bodies.

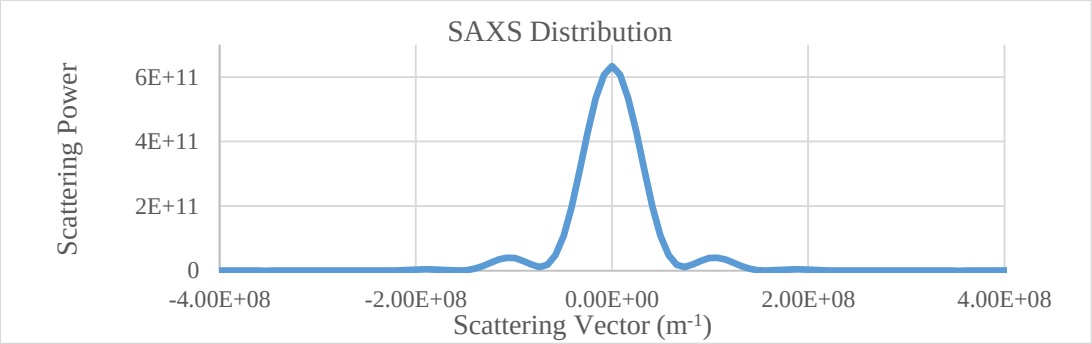

Figure 2.1 A SAXS distribution numerically calculated for a CNT model state used in the interpretation of data presented in chapter 4. The details of the calculation are also presented in chapter 4. The general features seen in this particular distribution are common to all SAXS distributions.

By the properties of the Dirac delta function

$$I_N(\vec{q}) = \frac{N}{V}|F|^2\left[\frac{|\Sigma(\vec{q})|^2}{\bar{v}} + \Phi(\vec{q})\right], \qquad 2.31$$

where $|\Sigma(\vec{q})|^2$ was treated as a delta function compared to $\Phi(\vec{q})$ because $\Phi(\vec{q})$ varies slowly as the scattering vector is varied. The scattering power for an arbitrary object has been decomposed into two terms. The first term depends on the size and shape of the object in that it only involves the transform of the form factor and represents a sharp peak about the origin of reciprocal space. The immediate neighborhood of the origin in reciprocal space corresponds to small scattering angles, so it is the shape and magnitude of this intensity peak that is measured in SAXS experiments. The second term involves the transform of the pair distribution function making it dependent on the particulate structure of the object. The second term is extended over reciprocal space and corresponds to scattering angles that are larger than those associated with the first term. SFHI relies on SAXS so only the first term needs to be retained for further discussion

$$I_N(\vec{q}) = \frac{N}{V}|F|^2\frac{|\Sigma(\vec{q})|^2}{\bar{v}} = \frac{|F|^2}{\bar{v}^2}|\Sigma(\vec{q})|^2. \qquad 2.32$$

At small scattering angles the form factor F is equal to the number of electrons in a constituent particle of the object, making equation 2.32

$$I_N(\vec{q}) = \rho^2 |\Sigma(\vec{q})|^2, \qquad 2.33$$

which is the general formula for the SAXS distribution of an object. Unfortunately this equation is only useful for the case of objects with high degrees of symmetry because the integrals involved become analytically intractable. Numerical methods must be resorted to in order to obtain SAXS distributions for more general objects.

The SAXS distribution of an object may be further divided into at least two more regions, the Guinier and the Porod. The Guinier region resides about the origin of reciprocal space, and may be approximated by an exponential function that also bears Guinier's name. The Guinier approximation depends on the radius of gyration of the scatterer. Therefore, the Guinier region contains information about the shape and size of the sample particles. The Porod region occupies higher spatial frequencies of reciprocal space relative to the Guinier region, and is defined as the part of the distribution that asymptotically decays as $|\vec{q}|^{-4}$. There exists an approximation of the Porod region that depends on the specific surface area of the sample particles. By plotting a SAXS distribution on a log-log (base 10) plot the Guinier and Porod regions may be identified. The Porod region will have a slope close to -4, and the Guinier region will lie closer to the origin of reciprocal space possessing a slope smaller than that of the Porod region.

Chapter 3 SFHI

3.1 Introduction

SFHI is an imaging modality that relies on the elastic scattering of X-rays into small angles to generate an absorption image and multiple scatter images from a single exposure[48-51]. The scatter images are sensitive to sample anisotropy. By modulating the spatial frequencies of an object with an absorption grid, the image may be subsequently demodulated by Fourier analysis resulting in images comprised of diffracted radiation. As long as the object remains sufficiently stationary while being imaged the edges of the object will be enhanced by phase contrast effects[52]. Conventional small angle X-ray scattering measures the scatter intensity distribution as a function of scattering angle. SFHI uses the illumination of the entire sample and absorption grid to measure the small angle scatter distribution at all locations in a sample simultaneously. Probing the small angle scatter distribution over the entire sample makes the SFHI scatter image intensity a measure of the integrated scatter distribution over some finite range of scatter angles determined by the experimental parameters.

Harmonic imaging possesses an increased sensitivity to variations in electron density than more common place X-ray imaging techniques such as X-ray absorption radiography or propagation based phase contrast imaging. Consider a sample of nanoparticles that undergo a small change in size at constant mass. Perhaps such a change has been effected by a temperature induced order-disorder transition in bi-metallic

nanoparticles or a block copolymer. Absorption imaging would be fairly insensitive to such a change in particle morphology because the change in absorption cross section could not be very significant. Phase contrast imaging relies on refraction at macroscopic interfaces and cannot detect small changes in nanoparticle particle size at constant mass. Previous studies have demonstrated SFHI's enhanced sensitivity to the presence of iron oxide[49] and gold[53] nanoparticle contrast agents over absorption radiography. Scatter images produced by SFHI contain phase contrast features in addition to the integrated scatter intensity and therefore contain information not accessed in pure phase contrast imaging.

3.2 Theory

SFHI imaging is implemented by placing an X-ray source, adsorption grid, object and detector in tandem.

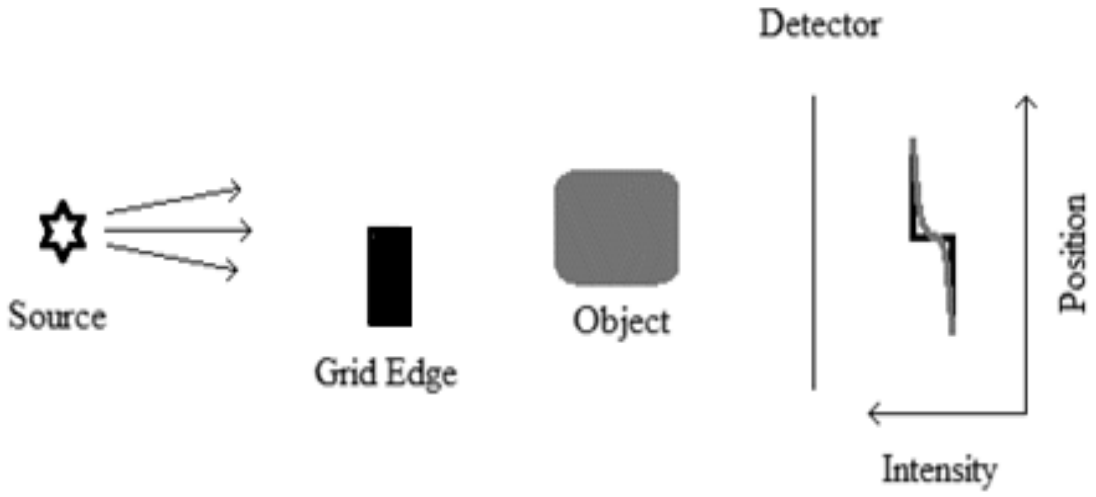

Figure 3.1 Schematic of SFHI experimental setup. The grid edge should be thought of as the cross-section of a single wire in a two dimensional mesh. At the far right the solid black line is the image of the grid edge projection when no object is present. The sigmoidal grey line is the blurred grid edge image. The blurring is due to radiation scattered by the object[54].

The recorded intensity is composed of radiation transmitted and diffracted by the object and grid. Scattering due to the object effectively blurs what would be a crisp grid projection onto the detector. Fourier analysis methods are implemented to extract a measure of the grid blurring and therein scatter from the object. SFHI is a table top imaging technique and can make use of common commercial polychromatic X-ray sources. While SFHI relies on small angle X-ray scattering it has the practical advantages of not requiring a monochromatic collimated X-ray beam typically provided by a synchrotron.

After an exposure of the grid and object is taken a fast Fourier transform of the image is computed to generate the object and grid reciprocal space. The grid is a two dimensional wire mesh so in reciprocal space it is represented as a two dimensional lattice of peaks located at the grid spatial frequency harmonics. The spatial frequency spectrum of the object is replicated about each grid harmonic peak. This can be understood in the limit of no scattering. In the absence of scattering the detected image is the product of intensities transmitted by the grid and object, which becomes a convolution in reciprocal space. The convolution of the two frequency spectra makes the reciprocal space a set of object spectrum replicas about each harmonic peak.

Let $F(\vec{x})$ be the object image and $G(\vec{x})$ be the grid image. In the absence of scattering the detected grid and object image is the product FG. If $f(\vec{q})$ and $g(\vec{q})$ represent the object and grid spectra, then the image spectrum is rigorously given by

$$\mathcal{F}\{FG\} = f(\vec{q}) * g(\vec{q}). \qquad 3.1$$

Convolution is denoted by the asterisk on the right hand side.

To generate harmonic images the Fourier spectrum of the grid and object image is multiplied by a low pass filter such that the entire spectrum is set equal to zero except for a small area about a chosen harmonic.

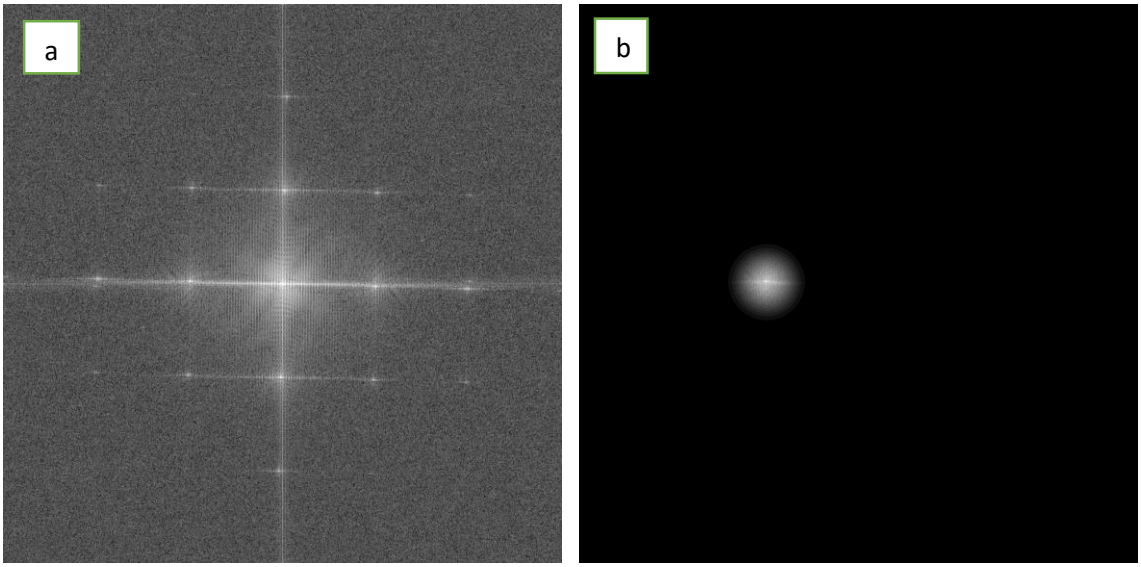

Figure 3.2 Figure **a.** is the fast Fourier transform of a grid image. The high intensity spots are peaks located at the spatial frequency harmonics of the grid. In **b.** a low pass filter has been applied to the entire reciprocal space of the grid image. Only the low frequencies relative to the first left horizontal/(1,0) harmonic are not set to zero. The width of the low pass filter is equal to the harmonic spacing. The inverse fast Fourier transform of the filtered spectrum is taken to produce a harmonic image.

The filtered Fourier spectrum is then inverse transformed to produce a demodulated object image. In the absence of scattering the harmonic images would be identical save for a variation in amplitude due to that of the corresponding grid harmonic. If the grid spectrum can be approximated as

$$g(\vec{q}) = \sum_{n_i,n_j} g_{n_i n_j} \delta\left(q_i - \frac{2\pi n_i}{P}\right) \delta\left(q_j - \frac{2\pi n_j}{P}\right), \quad n_i, n_j \in \mathbb{I}, \qquad 3.2$$

then the reciprocal space is

$$f(\vec{q}) * g(\vec{q}) = \sum_{n_i n_j} g_{n_i n_j} f\left(q_i - \frac{2\pi n_i}{P}, q_j - \frac{2\pi n_j}{P}\right) \quad 3.3$$

and the harmonic images are equal to the products

$$H_{n_i n_j}(\vec{x}) = g_{n_i n_j} F(\vec{x}). \quad 3.4$$

In equation 3.2 $g_{n_i n_j}$ is the amplitude of the harmonic identified by the horizontal and vertical integer indices n_i and n_j, P is the grid period, q_i and q_j are the components of the scattering vector $\vec{q}$ and δ is the Dirac delta function. To arrive at equation 3.4 the implicit assumption was made that the object spectrum is band limited

$$f(\vec{q}) = 0 \quad if \quad |\vec{q}| > \frac{\pi}{P}. \quad 3.5$$

By assuming a band limited object image the demodulated object image is recovered upon inverse transform of the filtered grid and object spectrum.

The peak located at the center of the image reciprocal space is unaffected by scattered radiation as its location corresponds to zero and near zero scattering angles. The harmonic image produced from the central harmonic is a conventional absorption radiography image. Due to the general decay of scattering factors with increasing spatial frequency higher harmonics are attenuated away from their transmission amplitude by scattered radiation. Attenuation of amplitudes at higher spatial frequencies away from those due to transmission is utilized to extract a signal proportional to the integrated scatter intensity.

All harmonic images are normalized by a corresponding harmonic image produced from an exposure of the grid alone in order to remove affects due to grid imperfections.

Assuming the grid spectrum may still be represented by equation 3.2 the (0,0) /absorption image is computed

$$S_{(0,0)} = -ln\left(\frac{g_{0,0}F(\vec{x})}{g_{0,0}}\right), \qquad 3.6$$

where $g_{0,0}$ is the magnitude of the central grid harmonic. Scatter images are computed

$$S_{(n_x,n_y)} = -ln\left(\frac{\frac{g_{n_i n_j}\tilde{F}(\vec{x})}{g_{n_i n_j}}}{\frac{g_{0,0}F(\vec{x})}{g_{0,0}}}\right) = -ln\left(\frac{\tilde{F}(\vec{x})}{F(\vec{x})}\right), \quad n_i \neq 0 \;\; and \;\; n_j \neq 0. \qquad 3.7$$

$\tilde{F}(\vec{x})$ is the object image whose spatial frequency spectrum was attenuated by scatter. A measure of object scattering is recovered from a single exposure by taking the ratio of a higher harmonic image to the central harmonic image because the object spectrum at higher harmonics should be altered by scatter relative to the scatter invariant object spectrum about the central harmonic. The negative natural logarithm is taken to make the final images linearly dependent on sample thickness.

There is a reduction in image quality between the original transmission image and images produced by SFHI. The decrease in image quality is due to filtering of the image spectrum. The filters are applied under the assumption that the object image is band limited, so the highest frequency feature visible in the processed images is $\frac{2\pi}{P}$. In other words the width of the applied filters is equal to the inter-harmonic distance so the resolution of the processed images is equal to the grid period.

The use of a two dimensional absorption grid allows scatter into those two dimensions to be distinguished, making SFHI sensitive to sample anisotropy. A brief visual

summary of SFHI and an example of its sensitivity to sample anisotropy are presented in Figure 3.3.

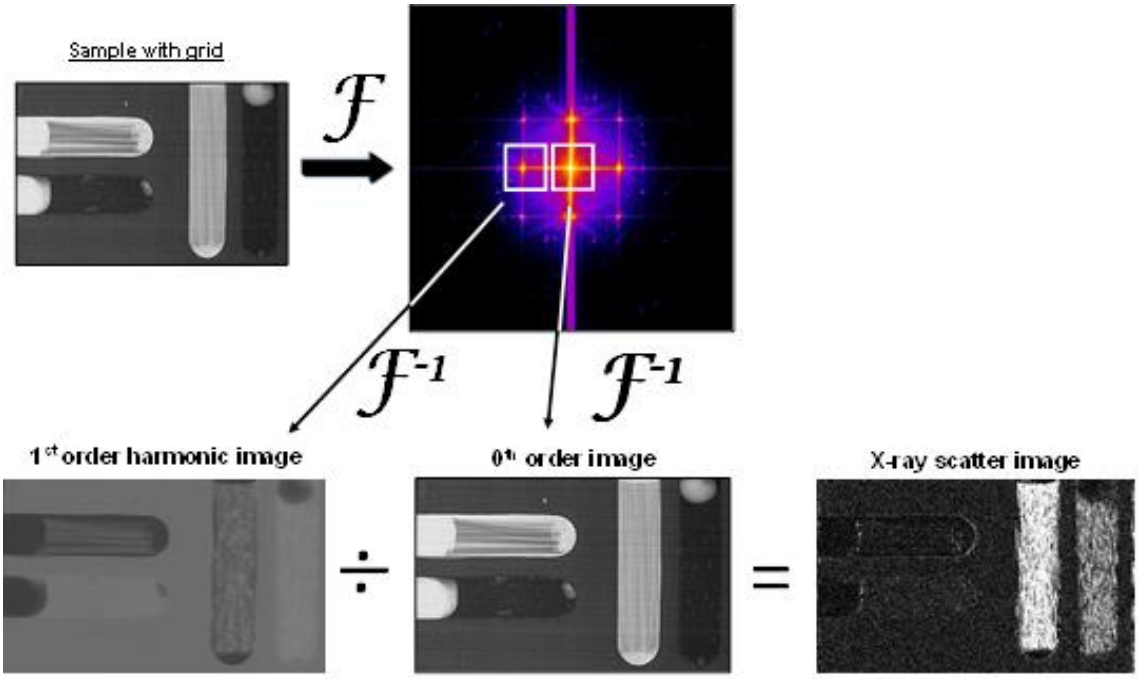

Figure 3.3 A sample and grid image is fast Fourier transformed to generate the image spectrum. The square regions about the (1,0) and (0,0) harmonics represent the application of low pass filters. Each harmonic is individually inverse transformed to generate a harmonic image, and the ratio of the harmonic images produces a scatter image. The samples in the image are aligned carbon fibers in glass tubes. By using the (1,0) harmonic scatter into the vertical direction is suppressed and only scatter into the horizontal direction survives.

3.3 Practice

3.3.1 Instrument Parameters

All of the X-ray data presented in this thesis were collected under the same experimental conditions. The X-ray source was a True Focus X-ray Tube, model TFX-

311EW with a tungsten anode and 10 um focus size. The detector was a 12 bit remote RadEye 200 CMOS camera with 96 um square pixels. The components of the imaging system were arranged vertically. The absorption grid was a stainless steel wire mesh. Details of the experimental system are displayed in the following table.

Experimental Parameter	Value
X-ray tube voltage	80 kV
X-ray tube current	0.2 mA
Grid pitch	150 lines per inch
Grid wire gauge	0.0026 inch
Source to detector distance	1.6 m
Object to detector distance	1.2 m
Exposure time	10 sec

Table 3.1 Experimental parameters used for the imaging system in all X-ray data presented in this thesis are listed with their numerical values.

3.3.2 The Algorithm

3.3.2.1 Image Processing Prior to Fourier Analysis

A novel algorithm was designed to carry out image processing. While the core of the algorithm remains the same as that first proposed by Han Wen[48] there were many decisions that had to be made on the periphery of his arguments. Another motivating factor in writing the image processing procedure was its automation. The data sets collected were often on the order of tens of Gigabytes and contained between 1,000 and 3,000 images. To process each image individually would permit too great a probability of human error in the results. The procedure was written in MATLAB.

The automated data acquisition will be discussed in a separate chapter, but for the current discussion it is pertinent to be aware of the files generated in that process. The data acquisition software saved all images as Tiff files with pixel values represented as 16 bit unsigned integers. The images collected were saved in a file directory and saved with names in the format *image* ***number time****sec* ***segment****.tif*. The italicized words are part of the file name common to every image while the bold and italicized words take on specific values. The index of the exposure since the start of the experiment is ***number***. The ***time*** is the time in seconds since the start of the experiment that the exposure time of the image was started. The ***segment*** is a general description of which experimental subset the image belongs to. For example if the experiment was comprised of a heating ramp followed by a cooldown period ***segment*** would be replaced by heat or cool. Once the experiment enters a new subset the index ***number*** and the ***time*** is reset. The image names are also saved in a separate text file called *image names.txt* to aid in their processing.

Prior to data acquisition a set of background, flatfield and grid images were taken. The background images are exposures with the X-ray tube turned off. The flatfield images are exposures with the X-ray tube turned on and nothing in the viewing field. The grid images are exposures of the grid alone. These setup images were saved in the same directory as the experimental images. The background and flatfield images were saved with file names in the format ***typeSetupNumber****.tif*. The ***typeSetup*** part of the file name is either background or flatfield, and ***Number*** is the index of the exposure. The grid images were saved with file names according to the format *grid* ***pitch*** *lpi****number****.tif*. The ***pitch*** is the number of lines per inch, which is why the characters *lpi* follow, and ***number*** is again the exposure index. The setup image names were also saved in the *image names.txt* file.

A setup text file called *setup.txt* was written prior to processing and contained information specific to the experiment and processing that will be mentioned when relevant. The image names file and setup file names are hard coded into the processing script because their names do not change across experiments. The processing script first accesses the setup file and reads the total number of images to be processed and the number of images to average over.

The script then starts to read the setup images into RAM by accessing the image names file. As the images are read into RAM the pixel values are typecast from 16 bit unsigned integers to double precision floating point numbers. The images are then passed through a median filter to remove dead and saturated pixels. For a given pixel the median filter examines the pixel intensity and the intensity values of the pixels in the immediate neighborhood. The pixel intensity of interest is replaced by the median intensity value of those considered.

Median filters typically use what is called an eight neighborhood. For locations removed from the pixel array borders there is no ambiguity in identifying eight pixels that touch the one under consideration. For pixels located at the array edge one method for generating an eight neighborhood is assigning pixel values in the actual neighborhood to artificial pixels in a way that the generated eight neighborhood has a mirror plane. The mirroring procedure and others like it essentially change the distribution of pixels values by weighting intensities without any reference to what the image features are. The median filter written as part of the SFHI algorithm only examines actual neighboring pixels, sorts the intensities and computes the median value to replace the pixel intensity

of interest. Obviously the case of odd and even numbers of neighborhood members had to be considered for each pixel when computing the median intensity value.

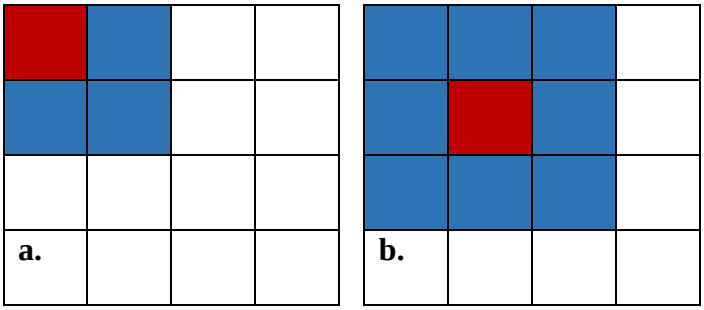

Figure 3.4 Both Figures **a.** and **b.** represent subsets of a pixel array. The pixel to which the medial filter written for the SFHI algorithm is being applied is colored red. The pixels in blue represent the neighborhood of pixels whose values are used in execution of the median filter.

Above Figure 3.4 displays an 8x8 subset of a pixel array. The red pixel in each image is the one being acted upon by the median filter, and the blue pixels constitute the neighborhood of that pixel. Both red and blue pixels are included in the calculation of the median intensity value.

Average flatfield and background images are generated for the purpose of correcting individual experimental and grid images by the formula

$$I_c = \frac{I-\bar{B}}{\bar{F}-\bar{B}}. \qquad 3.8$$

The experimental exposure or grid exposure is I, the average background image is $\bar{B}$, the average flatfield image is $\bar{F}$ and the background and flatfield corrected exposure is I_c.

The CMOS detector is an array of 1000x1024 pixels. Because the aspect ratio of the images is not equal to unity, upon taking the fast Fourier transform the spacing of the

grid harmonics in the vertical and horizontal directions are not equal. In order to regain a symmetric frequency spectrum with the correct inter-harmonic distances the background and flatfield corrected images are made square by adding 12 rows of pixels with zero intensity values at the top and bottom of the image.

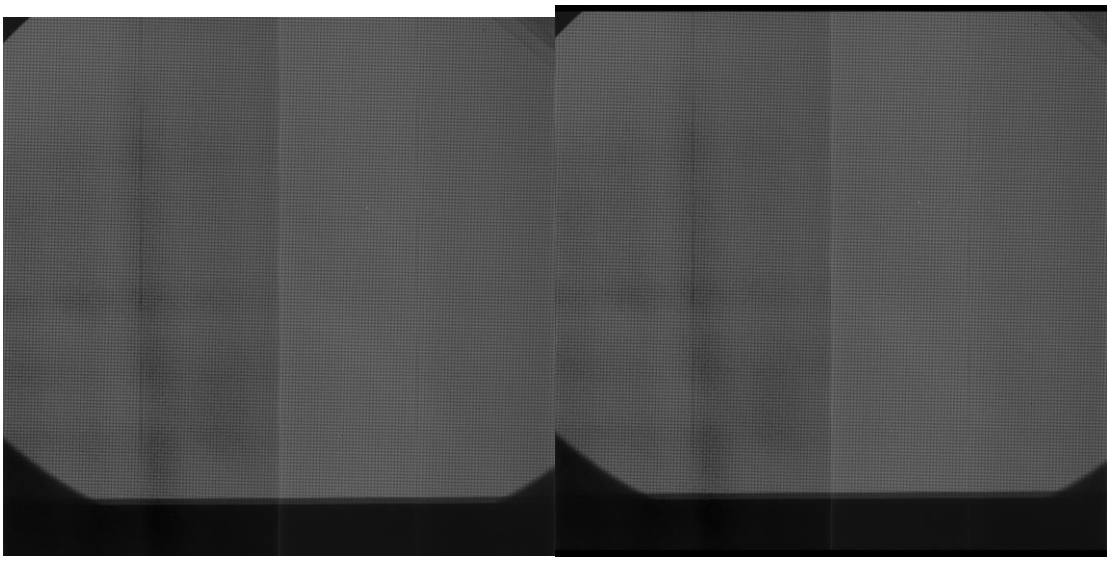

Figure 3.5 To the left is an exposure of the absorption grid with 1000 x 1024 pixels. To the right is the same image with 12 rows of zero intensity pixels artificially added to the top and bottom of the image to make it 1024 x 1024 pixels. Making the image square maintains the proper harmonic spacing in the vertical and horizontal directions of the image spectrum.

To reduce noise and the effects of image features not under study on further processing a region of interest is defined in the setup file. Pixels outside of the region of interest are set equal to zero.

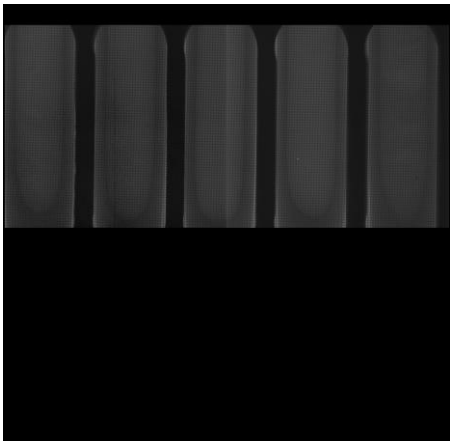

Figure 3.6 The region of interest defined in the setup file has been applied to an image of CNTs in glass vessels in an aluminum holder. Only the region of the image containing the CNTs will yield signals of interest, so the remainder of the image is set to zero intensity.

3.3.2.2 Fourier Analysis

After being typecast, median filtered, background corrected, flatfield corrected, made square and a region of interest identified the first experimental exposure is transformed and displayed for the user. The user is then prompted to select the first horizontal and vertical harmonics using the mouse. The user harmonic selection is used to generate a search area where a custom peak finding algorithm is implemented. The harmonic is found by searching for a maxima in an area about the point provided by the user input. The search area is chosen sufficiently small so the maxima found can only correspond to the intended harmonic peak. When located the left first order horizontal harmonic is marked with a blue asterisk and the first order vertical harmonic is marked with a red asterisk. The location of the first horizontal and vertical harmonics is then used to calculate the inter-harmonic distance. The angular deviations of the first order harmonics from the horizontal and vertical directions relative to the central harmonic are also

calculated. The inter-harmonic distance and angular deviations are subsequently used for the automatic placement of low pass filters referred to in section 3.2.

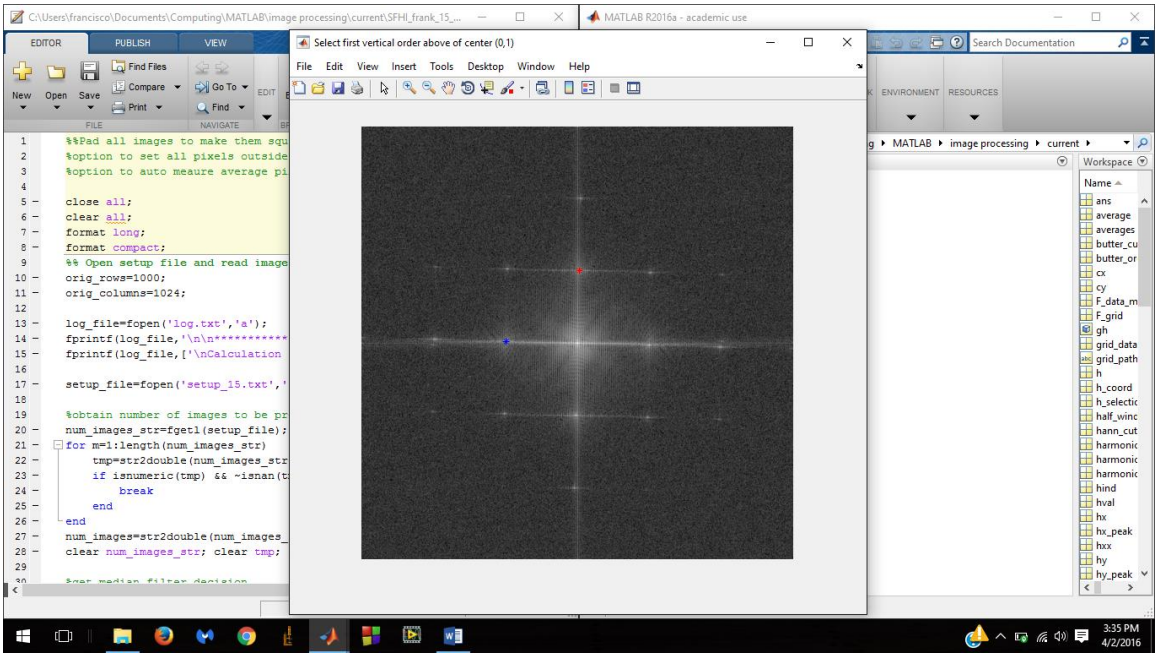

Figure 3.7 Screen shot of frequency spectrum presented to the user of the SFHI MATLAB script. The user is prompted by text at the top of the spectrum window to first select the (1,0) harmonic and then the (0,1) harmonic. After each selection a peak find algorithm is implemented and an asterisk is placed over the peak maximum. The locations of the harmonics are used to calculate the inter-harmonic distance and the angular deviation of the harmonics from the horizontal and vertical directions relative to the (0,0) harmonic.

After calculation of the inter-harmonic distance and angular deviations images are automatically processed. Each image is processed as previously described and then transformed. The harmonics that will be low pass filtered are listed in the setup file by a convention similar to Cartesian coordinates. For example (0,1) is the first vertical harmonic and (1,0) is the left first horizontal harmonic. The integer coordinates are multiplied by the inter-harmonic distance to generate a point in reciprocal space to center

the low pass filter. The position of the filter center also depends on the angular deviations of the harmonics. The low pass filter is then applied to the central harmonic and higher order harmonics one at a time, and the filtered Fourier spectra are inverse transformed to generate harmonic images. The modulus of the harmonic images is calculated to produce a real image.

The Fourier transformation has many properties that must be considered when it is applied, such as needing to make the image square in order to maintain the natural symmetry of the grid harmonics in the horizontal and vertical directions. The most important property of Fourier analysis to consider when choosing a low pass filter in the generation of harmonic images is the Gibbs phenomena. The Gibbs phenomena refers to the Fourier series of a piecewise smooth discontinuous function exceeding the function's limiting value at a jump discontinuity, resulting in oscillations of the function's Fourier series. These oscillations are a source of ringing in data processing. Gibbs phenomena is associated with the fast Fourier transform of a function that has been multiplied by a window function or filter, and is therefore an issue that must be addressed in the current work.

The low pass filter implemented was designed to minimize the Gibbs phenomena upon inverse transformation of the image spectra. The filter was a 14th order Butterworth Hann hybrid filter,

$$w = \begin{cases} \left[1 + \left(\frac{|\vec{q}|}{|\vec{q}_0|}\right)^n\right]^{-\frac{1}{2}}, & |\vec{q}| < |\vec{q}_0|3^{\frac{1}{n}} \\ \left[1 + \left(\frac{|\vec{q}|}{|\vec{q}_0|}\right)^n\right]^{-\frac{1}{2}} \cdot \left[\frac{1}{2} + \frac{1}{2}cos\left(\frac{\pi|\vec{q}|}{|\vec{h}_0|}\right)\right], & |\vec{q}| \geq |\vec{q}_0|3^{\frac{1}{n}} \end{cases} \quad 3.9$$

The first term of the piecewise function is a Butterworth filter and the second term is a Butterworth filter multiplied by a Hann filter. In the above equation w is the filter/window function, $|\vec{q}|$ is the spatial frequency relative to the harmonic of interest, $|\vec{q}_0|$ is the spatial frequency at which the Butterworth filter attenuates the gain to 70.7 percent of the maximum, n is the Butterworth filter order, $|\vec{h}_0|$ is the spatial frequency at which the Hann filter attenuates the gain to zero and $|\vec{q}_0|3^{\frac{1}{n}}$ is the spatial frequency at which the Butterworth filter attenuates the gain to 50 percent of the maximum. The Butterworth cutoff frequency $|\vec{q}_0|$ was chosen as 40 percent of the inter-harmonic distance, and the Hann cutoff frequency $|\vec{h}_0|$ was chosen as 50 percent of the inter-harmonic distance.

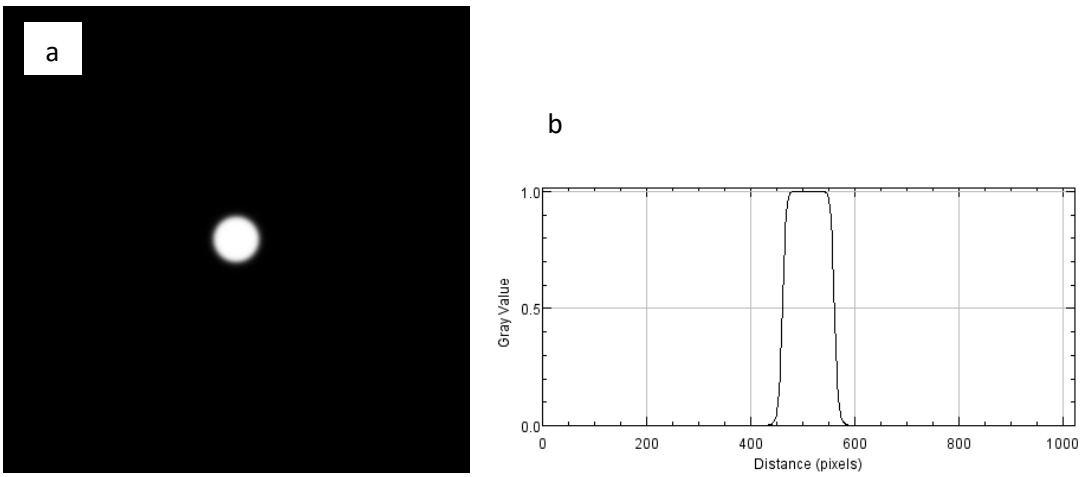

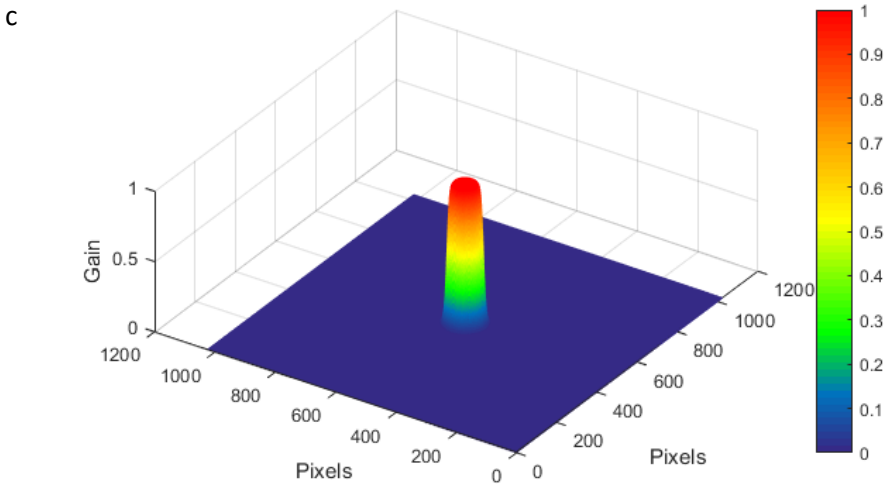

Figure 3.8 a. An image of the hybrid filter mask centered over the location of what would be the (0,0) harmonic. **b.** Cross-section of the filter mask shown in figure **a.**. **c.** The hybrid filter shown in figures **a.** and **b.** plotted as a surface. Spatial frequencies located within the red part of the filter are not attenuated, and spatial frequencies located within the blue part of the filter are attenuated to zero.

The hybrid filter used minimizes the degradation of image spatial frequency integrity and ringing due to Fast Fourier transformation better than either individual filter. Higher spatial frequencies relative to a given harmonic become less attenuated as the Butterworth filter order increases, and in the limit of infinite order a radially symmetric Butterworth filter is equal to a right cylindrical filter and produces a jump discontinuity. If the Butterworth order is made too high the attenuation of spatial frequencies within the filter domain is minimized, but the rate of gain attenuation at the filter boundaries is sufficiently similar to a jump discontinuity that ringing may be observed in the resultant images. The order of the Butterworth filter was chosen to be as large as possible without re-introducing the Gibbs phenomena that would result from a simple right cylindrical shaped filter. The Hann function's contribution to the filter forces the window function to

smoothly decay to zero avoiding ringing produced by a jump discontinuity as a result of truncating the window function at 50 percent of the inter-harmonic distance. After application of the hybrid filter and Fourier inversion of the spectra, the harmonic images are further processed as described in section 3.2 to generate an adsorption image and the specified scatter images.

The setup file contains the number and location of different image subsets termed sample regions. The average pixel intensity is calculated for each of the different sample regions in the original transmission images, the absorption images and each of the scatter images. A further average is then calculated over a set of images containing the number of images to average over, gotten from the setup file. The standard deviation of the average intensity is also calculated across the same sets of images. The averages and standard deviations are then stored in RAM until all images have been processed, at which point the values are written to text files.

3.4 Calibration

In order to determine the sensitivity limit of the imaging system the scatter from spherical gold nanoparticles was used to find the minimum scattering angle probed. Dr. Danielle Rand, a former Rose-Petruck group member, purchased gold nanoparticles with diameters 2 nm, 5 nm, 10 nm, 50 nm and 100 nm from BBI (Cardiff, UK), imaged the particles and did the data analysis. I compared Dr. Rand's experimental observations to numerical calculations of integrated SAXS distributions to find the minimum scattering angle our imaging system was sensitive to. The nanoparticles came stabilized in citrate

and were not subject to any further modification. The nanoparticle sizes were confirmed with a Zetasizer Nan ZS from Malvern Instruments (Malvern, UK). The Zetasizer measures the hydrodynamic diameter of the nanoparticles by subjecting the suspension to dynamic light scattering (DLS). The concentration of gold in each purchased suspension was determined by Inductively-Coupled Plasma Atomic Emission Spectroscopy (ICP-AES).

Figure 3.9 Gold nanoparticle suspensions. The gold particles have diameters of 2 nm, 5 nm, 10 nm, 50 nm and 100 nm from left to right. The difference in color is due to the change in surface plasmon resonance with particle diameter[55].

The manufacturer specifications and those determined by Dr. Rand are presented in the following table.

	Size, from BBI (nm)	Size, DLS (nm)	[Au], from BBI (ppm)	[Au], ICP-AES (ppm)
2 nm	N/A	177 ± 22.6	12.1	11.7± 0.12
5 nm	5 ± 0.8	10 ± 1.3	63.2	62.5 ± 1.66
10 nm	10 ± 1.0	12 ± 0.8	57.6	65.3 ± 1.69
50 nm	50 ± 4.0	60 ± 3.0	56.8	58.2 ± 0.22
100 nm	100 ± 8.0	103 ± 4.3	56.6	56.0 ± 1.09

Table 3.2 Gold nanoparticle diameters and concentrations as provided by the manufacturer BBI and as measured by Dr. Rand using dynamic light scattering (DLS) and Coupled Plasma Atomic Emission Spectroscopy (ICP-AES). The 2 nm gold nanoparticles are poorly characterized for reasons discussed in the text[55].

BBI determines nanoparticle size by TEM. DLS includes the ion layers formed on the nanoparticle surface in suspension in the determination of diameter, which accounts for the consistently larger values found by DLS compared to those reported by BBI. The diameter found by DLS for the 2 nm diameter particles suggests that they aggregated to form large clusters. The manufacturer recommended a minimum concentration of 500 ppm when conducting size measurements on particles with diameter less than 10 nm. The less than recommended concentration of the 2 nm solution could have also effected the measured diameter.

All particle solutions except for the 2 nm solution were diluted to 50 ppm for imaging. The 2 nm solution was used as-purchased. The imaging experimental parameters are contained in the table in section 3.2.1, except that the exposure time was 20 seconds. Two sets of images were collected with the prepared solutions. In the first experiment all five solutions were imaged simultaneously, and permuted in the viewing field to negate

any heterogeneity in the sensitivity of the detector. Three images were taken for each of the five permutations for a total of 15 exposures. The scatter signals were averaged over all 15 exposures, divided by the corresponding absorbance signal and divided again by the absorbance normalized 2 nm diameter scatter signal. The results are displayed in Figure 3.10 a.

In the second experiment the suspensions were imaged individually with water as a control. Three images were taken of each suspension. An average of the scatter signals was taken over the three exposures, the signal was divided by the corresponding absorbance signal and then divided by the absorbance normalized water scatter signal. The signals were then again normalized by the 2 nm diameter signal. The results are displayed in Figure 3.10 b.

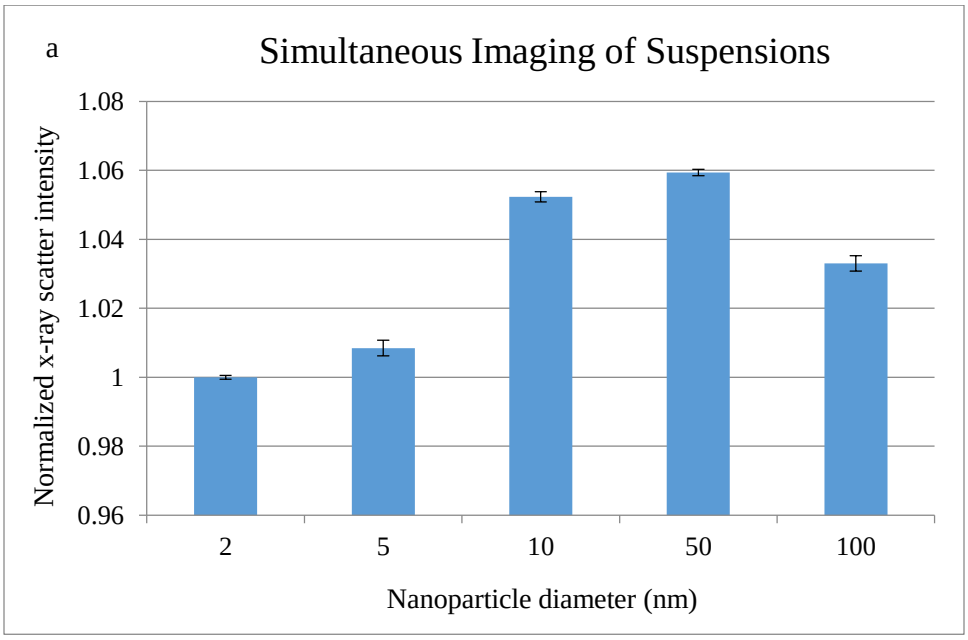

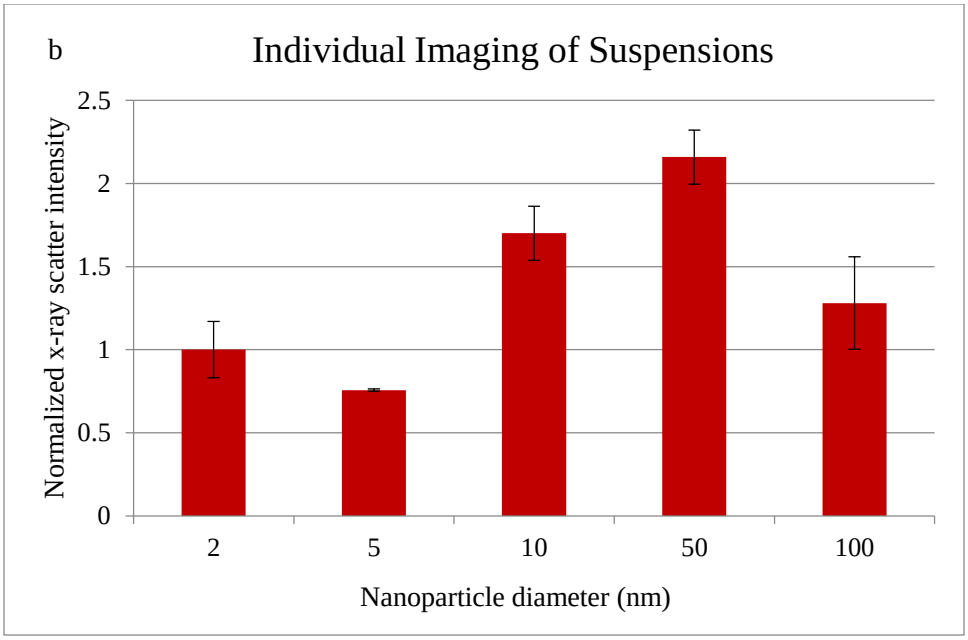

Figure 3.10 Scatter intensity for nanoparticle solutions of different diameters as a result of imaging all suspensions simultaneously and permuting their positions in the viewing field **a** and imaging each suspension individually with water as a control **b**. The scatter intensities were normalized by their corresponding absorbance signals and then to the 2 nm diameter scatter signal. The scatter intensities of the suspensions imaged individually were also normalized to the signal from the water control. The error bars are one standard deviation of the mean[55].

The 50 nm gold particles scattered the strongest for the experimental parameters followed by the 10 nm, then the 100 nm and finally the 5 nm particles. Due to the remaining ambiguity in the size measurement of the 2 nm particles they were not used in the calibration of the imaging system because the data collected may not be representative of the scattering properties of a well dispersed suspension of 2 nm spherical gold particles. The numerical values for an average taken over the normalized scatter data for images taken of the suspensions simultaneously and imaged individually against water are given in the following table.

Nanoparticle diameter	2 nm	5 nm	10 nm	50 nm	100 nm
Normalized x-ray scatter signal enhancement (%)	0.0 ± 0.16	0.3 ± 0.08	3.0 ± 0.18	3.6 ± 0.17	1.8 ± 0.28

Table 3.3 The average scatter enhancement relative to that of the 2 nm diameter particle suspension. An average was taken over the integrated scatter intensities shown in Figures 3.9 a and b[55].

In section 2.2 it was shown that the small angle X-ray scatter distribution for a statistically homogeneous object is given by equation 2.33

$$I_N(\vec{q}) = \rho^2 |\Sigma(\vec{q})|^2,$$

and that this expression is only useful in the case of objects with high degrees of symmetry. Spherically symmetric bodies possess the highest degree of symmetry amongst geometric objects in Euclidean space so the above formula will yield an analytical expression for the scattering power. The form factor for a spherical body of radius r is

$$\sigma(\vec{x}) = \begin{cases} 1, & |\vec{x}| \leq r \\ 0, & |\vec{x}| > r \end{cases}. \qquad 3.10$$

Then

$$\Sigma(\vec{q}) = \int_V e^{-i\vec{x}\cdot\vec{q}}\, dv, \qquad 3.11$$

where V is the volume of the spherical particle. Carrying out this integral in spherical polar coordinates and using it in the expression for the scattering power gives

$$I(\vec{q}) = \left[(\rho - \rho_0)\frac{4}{3}\pi r^3\right]^2 \left[\frac{9(\sin(rq) - rq\cos(rq))^2}{(rq)^6}\right], \qquad 3.12$$

where ρ is the electron density of gold, ρ_0 is the electron density of water, r is the particle radius and q is the norm of the angular spatial frequency vector. The difference in electron densities of gold and water is taken because the particles are in a suspension.

Even though the integrated scatter signals were normalized by the absorbance signals this only accounts for variations in gold concentration, but not in the variation of nanoparticle number giving rise to the diffracted intensity. Equation 3.12 was calculated for each size nanoparticle and multiplied by the number of nanoparticles that can be constructed from the amount of gold in a single 100 nm particle. The scatter distributions weighted by the number of particles relative to the 100 nm sample were then numerically integrated. The integral as a function of upper integration limit, decreasing scattering angle, was plotted. The use of equation 3.12 implies that the nanoparticles scatter independently of each other. This assumption is sometimes called the widely separated particle approximation and was invoked. The average distance between nanoparticles was calculated for each suspension and compared to the coherence length of the X-ray tube. The coherence length is the maximum distance between two scattering bodies such that light diffracted by the two bodies will still interfere to an appreciable degree. Therefore if the average distance between two nanoparticles is close to or greater than the coherence length the nanoparticles will essentially scatter independently of each other and can be considered as widely separated. The coherence length of the X-ray tube was calculated to be 1.6 um. The average distance between the 5, 10, 50 and 100 nm diameter nanoparticles was calculated to be 0.3, 0.6, 3 and 6 um respectively.

The integrated scatter distributions for the gold nanoparticle solutions are shown in Figure 3.10. The total range of angles considered in generating the SAXS distributions was

[0,0.08] radians. Given the experimental geometry 0.08 radians corresponds to 9.6 cm at the detector plane which is equal to the width of the detector in the smaller dimension. Only pixels at the detector edge would capture radiation scattered into this angle by points in the sample located under the opposite side of the detector. Therefore radiation scattered into the upper angular limit contributes negligibly to the overall scatter signal. Also given that a small angle scatter distribution is always a narrow peak about the origin of reciprocal space it is generally true that only amplitudes at angles closer to zero will contribute significantly to the integral.

Qualitative agreement with the measured scatter signals is achieved around 0.0795 radians. The abscissa is misleading. The lower limit of integration was 0.08 radians and the upper limit was varied towards zero. The value of 0.07925 radians actually corresponds to the integrations being carried out with a lower limit of 0.08 radians and an upper limit of 7.5×10^{-4} radians. Therefore, the smallest scattering angle to which the imaging geometry was sensitive was 7.5×10^{-4} radians. The minimum scattering angle corresponds to a distance in the detector plane equal to about 9 pixels. The grid period at the detector plane is about 7 pixels, so the minimum scattering angle to which the imaging was sensitive corresponded to radiation deflected a distance approximately equal to a single line pair of the grid image. The emission spectra for the X-ray tube was calculated using the SpekCalc software package[56-58]. The average wavelength was found to be 0.4 angstroms using the emitted intensities as statistical weights. The significance of the minimum scattering angle probed by SFHI with respect to data interpretation will be discussed in chapter 4.

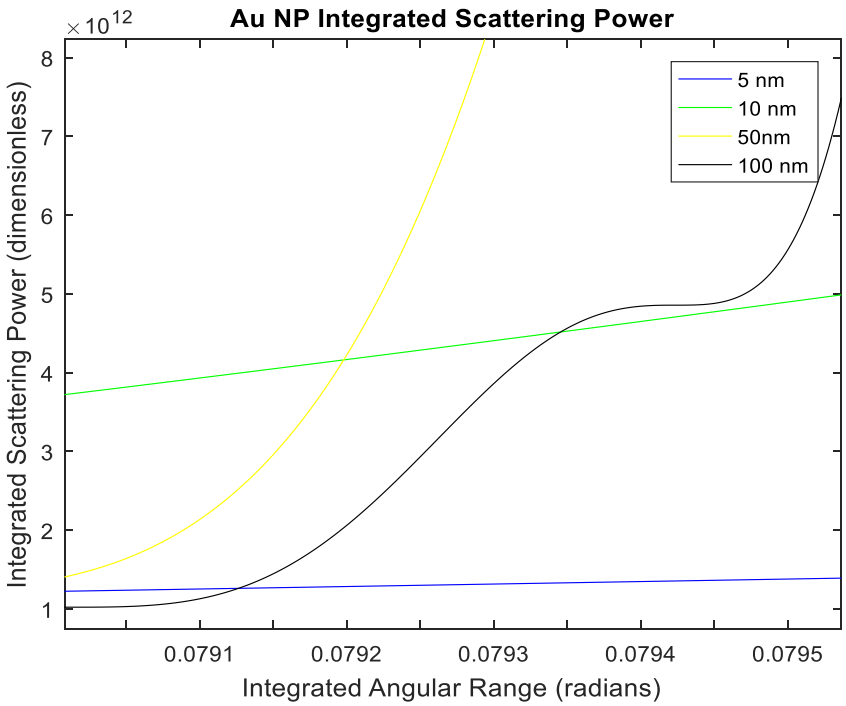

Figure 3.11 Integrated scattering power for gold nanoparticles of different diameters as a function of minimum scattering angle. Qualitative agreement with the trends seen in figure 3.9 is achieved around 0.07925 radians, which means that the minimum scattering angle to which the imaging system was sensitive is 7.5×10^{-4} radians. The lower limit of integration was 0.08 radians.

Chapter 4 SFHI of Aqueous Phase Transitions Inside Multi-Walled Carbon Nanotubes

4.1 Sample Preparation

The evaporation and condensation of water on multi-walled carbon nanotube surfaces was studied as a function of temperature, time and chemical functionalization using SFHI. MWCNTs produced by chemical vapor deposition were purchased from Nano Lab Inc. (Waltham, MA). The synthesis closely followed that of Li *et. al.*[59] The inner and outer diameters were reported as 7 ± 2 nm and 15 ± 5 nm respectively. The tube length was 1-5 um.

A fraction of the MWCNTs were placed in a Pyrex tube open to atmosphere and heated to 500 ^{o}C for 50 minutes to remove hemispherical caps sealing the tube ends and to functionalize the tube walls with oxygen containing functional groups.[12, 60-65] Carbon nanotubes are often sealed at their ends by hemispherical caps. These caps are more reactive than the cylinder walls which causes that caps to degrade faster than the tube walls in an oxidative environment. Heating produced a 15% mass loss.

Two functionalized and two as-purchased 16 mg samples of the MWCNTs were placed in glass tubes. The CNTs were packed at one end of the glass tubes by a glass wool plug, and 250 ul of nano-pure water were added to one functionalized and one as-purchased sample. All four samples were then vacuum sealed and placed in an aluminum holder fitted with two heating elements, a thermocouple, and five sample slots. The middle slot

contained an empty glass tube. The two samples that did not have water explicitly added were heated to 110 ^{o}C for ten minutes while under vacuum in order to insure that all water already adsorbed into the CNTs was removed. The portions of the glass tubes containing CNTs were within the dimensions of the holder, while the empty lengths of glass tubing that remained extended beyond the holder. Extension beyond the dimensions of the aluminum holder allowed the vacant portion of the glass tubes to remain at room temperature throughout the experiment. The dry samples were therefore under vacuum while the wet samples were under a pressure equal to that of water vapor pressure at room temperature.

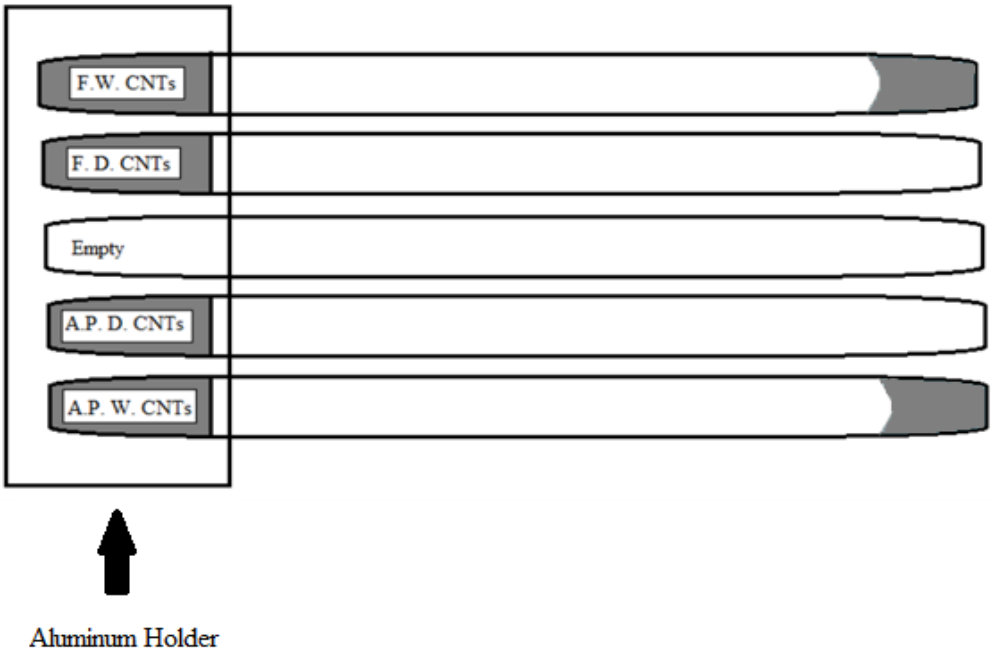

Figure 4.1 Schematic of sample arrangement. F. stands for functionalized (heat treated), A.P. stands for as-purchased, W. stands for wet and D. stands for dry. The CNTs were placed in glass tubes and then vacuum sealed. The portions of the glass tubes within the aluminum holder are within the viewing field of the imaging system. The aluminum holder was heated during the experiments, so the portions of the glass tubes that extend beyond the aluminum holder remained at room temperature[54].

Only the sample volumes contained within the dimensions of the aluminum holder were in the viewing field of the imaging system. As the samples were heated a temperature gradient was established and water condensed at the room temperature end of the glass tubes out of the viewing field.

Prior to imaging the samples were situated in a vertical position to ensure contact of the CNTs with the added water. The samples were then oriented horizontally and heated to 80^{o} C for 30 minutes to expel excess water from the samples into the region of the glass tubes outside of the viewing field. After preheating the samples were allowed to cool for four hours.

4.2 Automated Data Collection

A LabView VI was written in order to integrate the CMOS detector, an OMEGA temperature controller and National Instruments chassis for the purpose of automating data collection. The user interface specifies the exposure time of each image, the pitch of the grid used in imaging, the number of images per set (which was called the number of images to average over in the image processing MATLAB script), the time that should elapse between image sets, the total length of the experiment, the high and low temperature set points and the time it should take to reach the temperature set points.

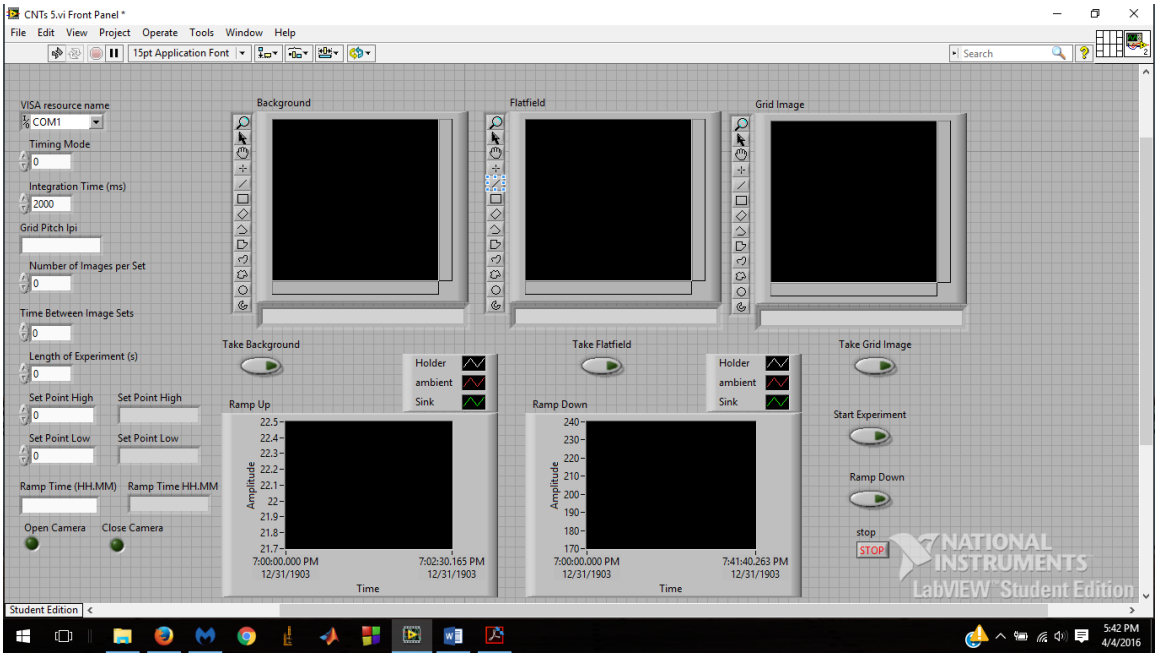

Figure 4.2 Screenshot of the LabVEIW virtual instrument written to automate the collection of X-ray images and temperature data. A number of experimental parameters are specified by the user in the labeled fields at the left of the front panel. As the images are read from camera memory they are saved to file and displayed in the labeled windows. The temperature data is plotted against time in the lower two windows.

Push buttons allow the user to specify when to record the setup images. The X-ray tube should be allowed to come to thermal equilibrium over a 30 minute period, so after the background exposures are taken the X-ray tube can be turned on and allowed to come to thermal equilibrium before pressing the push button called *Take Flatfield.* The push button triggers the camera to record the correct number of flatfield exposures. The X-ray tube then has to be turned off, the absorption grid placed in the viewing field and the X-ray tube turned back on. When the X-ray tube is again at thermal equilibrium the camera will be triggered by pressing the push button named *Take Grid Image*. The same set of steps is then followed for placing the sample in the viewing field and starting the experiment. As the images are recorded they are read from the camera memory as RAW

type images, converted into TIFF files and saved to a file directory specified by the user in a dialog window presented when the VI is started. The file naming convention employed was previously described in section 3.3.2.1. The text file containing a list of the image names is also in the same directory and written by the VI as the images are collected. The temperatures recorded by the National Instruments chassis are also written to a text file called *temp profile.txt* along with the experimental time at which they were recorded.

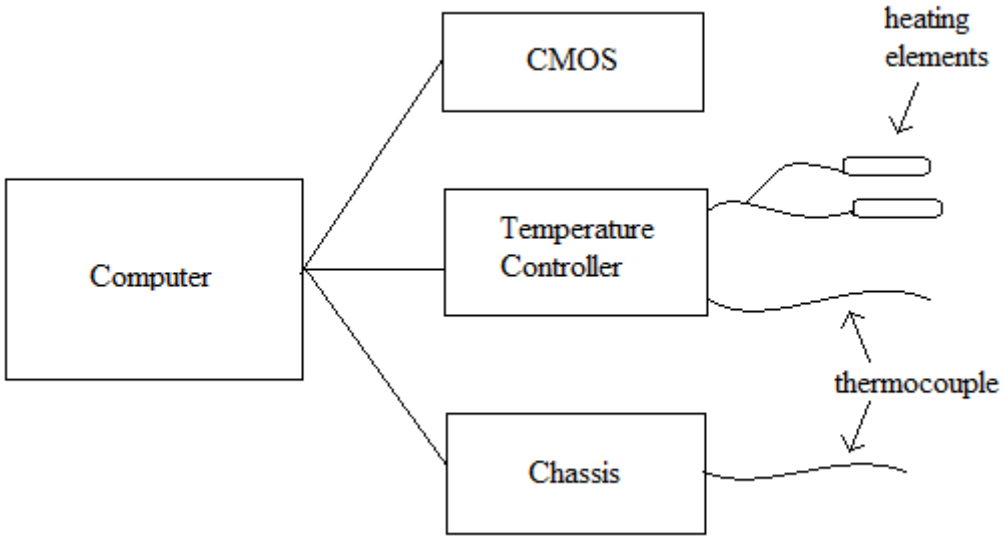

Figure 4.3 Schematic of instrument integration in order to automate data collection. A LabVEIW VI coordinates the acquisition of X-ray images from the CMOS detector and temperature measurements from the National Instruments chassis. After writing the temperature set point, and perhaps the ramp time, to the temperature controller it acts independently to control the temperature of the aluminum block holding the samples. The thermocouple connected to the temperature controller only provides the process variable for PID control over the aluminum block temperature.

The temperature controller was a CNi3244-C24 model controller from OMEGA Engineering. The controller had an 8 bit processor and therein was incapable of simultaneously executing a temperature ramp and recording the temperature values

measured by its thermocouple. The thermocouple connected to the controller was only used as a means of obtaining a process variable for the PID control of the heating elements during a temperature ramp. In order to record the temperature the National Instruments chassis was used with an NI 9219 module.

Two separate experiments were conducted using the prepared samples. In the first experiment the samples were heated as quickly as possible to a set point temperature that was then maintained. The set points covered were 45 ^{o}C, 60 ^{o}C, 85 ^{o}C and 95 ^{o}C. Equilibration at the set points never took longer than three minutes. In the second experiment both evaporation of water from the samples and condensation of water back into the samples were monitored by application of a 1 hour heating ramp to 320 ^{o}C followed by a cooling period where the samples radiated heat. In both experiments sets of 5 exposures 10 seconds in length were taken at regular intervals between temperature measurements. Scatter images were then produced by processing the recorded exposures. Only the first vertical harmonic was used because the edges of the aluminum holder and glass tubes were aligned vertically in the images causing the horizontal harmonics to contain scatter from these features. The difference in average intensities between samples containing water and their corresponding dry sample were taken to correct for any change in the detector sensitivity.

4.3 Results

The absolute intensities generated by SFHI analysis have little physical significance compared to the change in intensity with time. The intensities detected are a function of photon flux, the analogue to digital conversion process and contain transmitted and

scattered radiation from the aluminum holder and glass tubes. Figure 4.4 contains the results of heating the samples to various set point temperatures. In the legend F refers to the samples that were functionalized by heat treatment, and AP refers to the as-purchased samples. The signals depicted are the differences between the intensities measured for the samples containing water and their corresponding dry samples, so any change in intensity is due solely to the effect of added water. The abscissa was normalized to the time at which all water had been removed from the as-purchased CNTs. The time in hours to which the abscissa was normalized is located next to the temperature at which images were collected.

The left ordinate is the scale for image intensities obtained from the (0,0) harmonic, so these intensities are due to changes in absorbance and have been rescaled to represent the amount of water in the samples as a percentage of the initial water content. A rescaling of absorbance values is permissible because absorbance is proportional to concentration. No such rescaling is permissible for the integrated scatter intensities, whose scale is the right ordinate. Scattered intensity is only related to the number of scattering centers squared in the zero scattering angle limit[46]. Both the scatter and absorbance intensities were offset corrected.

In each of the four graphs shown in Figure 4.4 the absorbance intensities decrease monotonically in accord with water leaving the viewing field. The integrated scatter intensity profiles for the functionalized and as-purchased samples are qualitatively the same at each temperature with an initial increase in intensity, followed by a subsequent increase, and then decrease back to baseline. A change in integrated scatter intensity for both samples is not observed until 20 to 30 percent of the water has been evaporated from

the CNTs, indicating that unlike absorbance the scatter intensity is not sensitive to the change in water content alone.

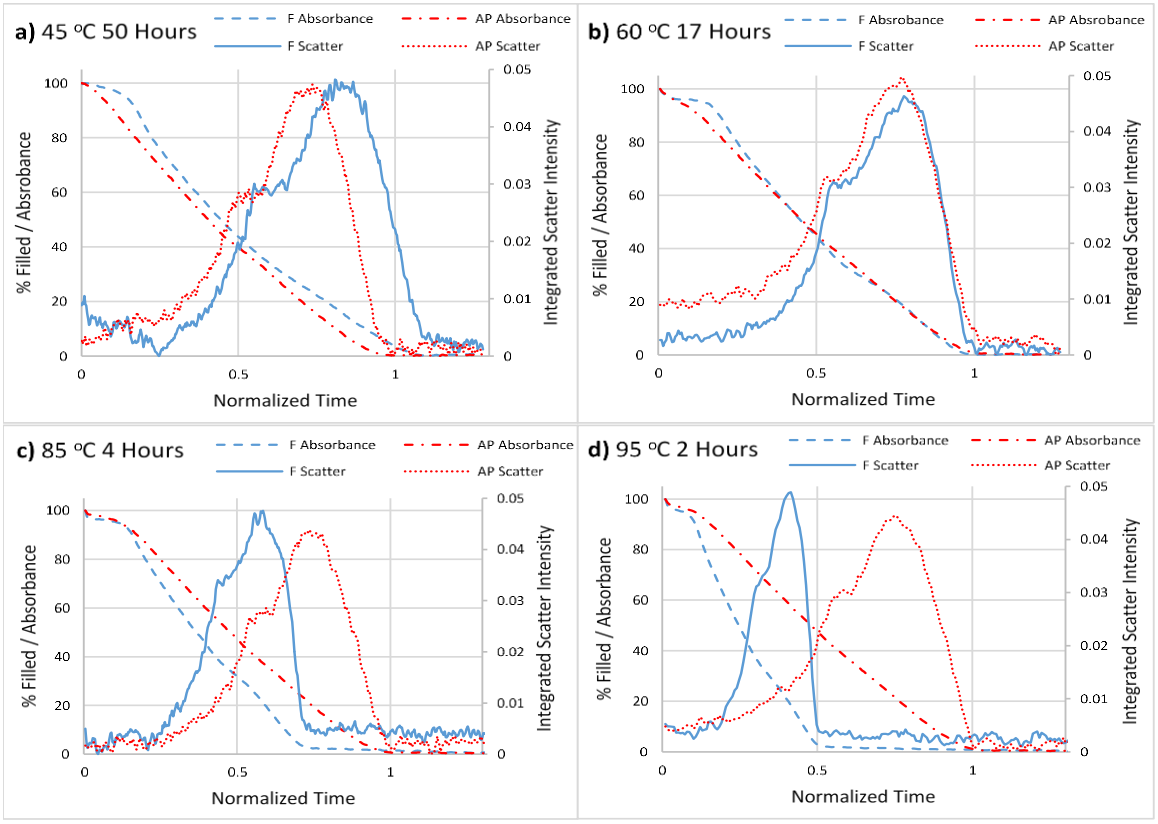

Figure 4.4 Results of SFHI analysis on X-ray images of CNTs heated to different set point temperatures that were then maintained. The heat treated/functionalized sample is labeled as F, and the as-purchased sample is labeled AP. The left ordinate is rescaled absorbance values that represent the percent filling of the CNTs relative to the initial water content. The right ordinate is the integrated scatter intensity scale. The abscissa is time normalized to the when evaporation in the as-purchased sample went to completion. The time to which the abscissa was normalized is next to the set point temperature in each figure. The signals shown are the differences of the signals from the wet samples and the signals from their corresponding dry samples. All signals have been offset corrected[54].

At 45 ºC (Figure a 4.4) and 60 ºC (Figure 4.4 b) water starts to evaporate from the as-purchased sample at an earlier time than the functionalized sample, and at 85 ºC (Figure 4.4 c) and 95 ºC (Figure 4.4 d) water starts to evaporate from the as-purchased and functionalized samples at about the same time. At all temperatures regardless of when evaporation begins water leaves the functionalized samples at a faster rate. Table 4.1 contains ratios of the slopes obtained from linear fits of the absorbance signals from 0.2 to 0.5 normalized time at each temperature.

Temperature (^{o}C)	$\frac{\text{Slope F}}{\text{Slope AP}}$	$\left(\frac{\text{Slope AP}}{\frac{\%\ \text{Filled}}{\text{Normalized Time}}}\right)$
45	1.079	-124.2
60	1.208	-120.88
85	1.233	-132.14
95	1.500	-123.66

Table 4.1 Slopes of the absorbance data presented in Figure 4.4 between 0.2 and 0.5 normalized time. The ratio of the change in the functionalized sample absorbance to the as-purchased sample absorbance demonstrates that for each set point temperature evaporation from the functionalized sample occurred more rapidly than in the as-purchased sample[54].

The change in evaporation rates between the functionalized and as-purchased samples with temperature is clearly seen in the absorbance profiles, but is also dramatized by the displacement of the scattering profiles relative to one another. At 85 ºC and 95 ºC the

increased evaporation rate of water from the functionalized sample compresses the scatter intensity profiles in time relative to the as-purchased sample.

Figure 4.5 contains the results of the second experiment where the CNTs were heated and then allowed to cool. The absorbance signals for both samples again monotonically decrease as water leaves the viewing field upon heating, and monotonically increase during condensation. Condensation occurred at about 70 ^{o}C in the functionalized sample and 40 ^{o}C in the as-purchased sample. The integrated scatter profiles during heating are similar in shape to those found in the experiments conducted at different set point temperatures except that they are compressed in time due to the rapid heating rate. During condensation the as-purchased scatter profile has a peak like shape while the functionalized scatter profile merely shows an abrupt increase. The difference between the two scatter signals is due to a lack of control over the degree of filling.

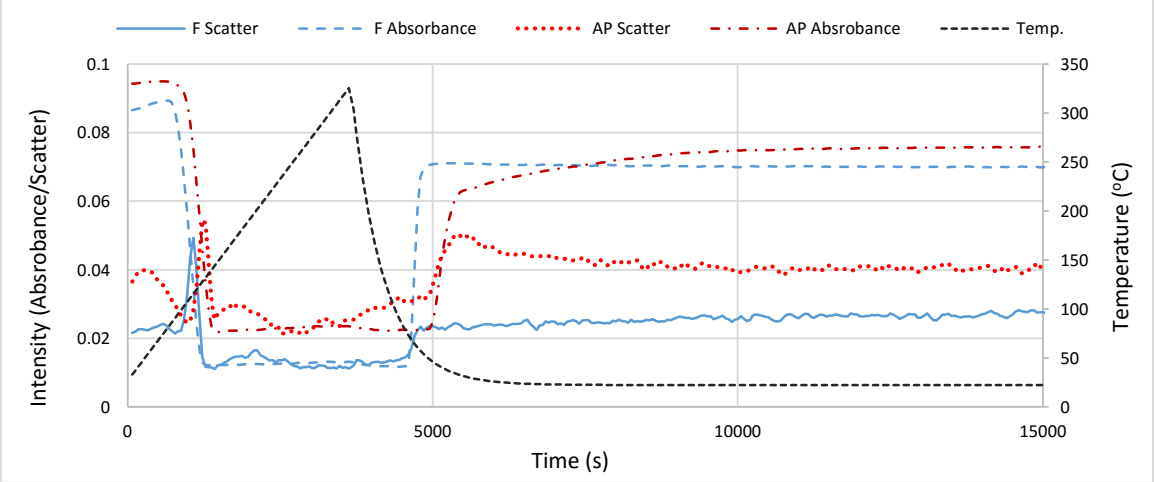

Figure 4.5 Results of SFHI analysis on X-ray images of CNTs heated to 320 ^{o}C that were then permitted to cool by thermal radiation. The functionalized sample is labeled F and the as-purchased sample is labeled AP. The left ordinate is intensity for both absorbance and scatter and the right ordinate is a temperature scale. The signals shown are the differences between the samples containing water and their corresponding dry samples. All signals have been offset corrected[54].

4.4 Interpretation

4.4.1 The Effect of Functionalization on Evaporation and Condensation

Functionalization of the CNTs by oxidation served to delay the evaporation of water from the inner pore of the CNTs at low temperatures, and to increase the temperature at which adsorption could take place. Evaporation from the functionalized sample is not seen to progress to any significant extent until 5 hours after the start of the experiment conducted at 45 ^{o}C (Figure 4.4 **a**). Such a long period of time precludes the conclusion that the samples are not at thermal equilibrium leaving only the presence of functional groups as the cause for delayed evaporation.

At elevated temperatures the augmented interaction of the functionalized CNTs with water is overcome by increased thermal energy, and water from both the functionalized and as-purchased samples start to evaporate at the same time. The increased evaporation rate from the functionalized sample seen at all temperatures (Table 4.1) is caused by uncapping of the CNTs and exaggeration of wall defects allowing for the escape of a larger number of water molecules per unit time. At temperatures where evaporation has gone to completion water vapor incident on the CNT surfaces constantly adsorbs and desorbs. When the samples were allowed to cool the presence of polar functional groups on the oxidized CNT surfaces permitted permanent adsorption at a higher temperature relative to the as-purchased CNTs.

4.4.2 Explanation for the Shape of the Integrated Scatter Profile during Condensation

In an effort to interpret the shape of the scatter intensity profiles in terms of CNT shape and water content the integrals over SAXS distributions corresponding to the four

states of CNTs observed in reference 13 were calculated. Figure 4.6 depicts the CNT model states used to compute SAXS distributions, and Figure 4.7 contains the results of taking the integral over each calculated distribution. The SAXS distribution for State 1 was already presented in Figure 2.1.

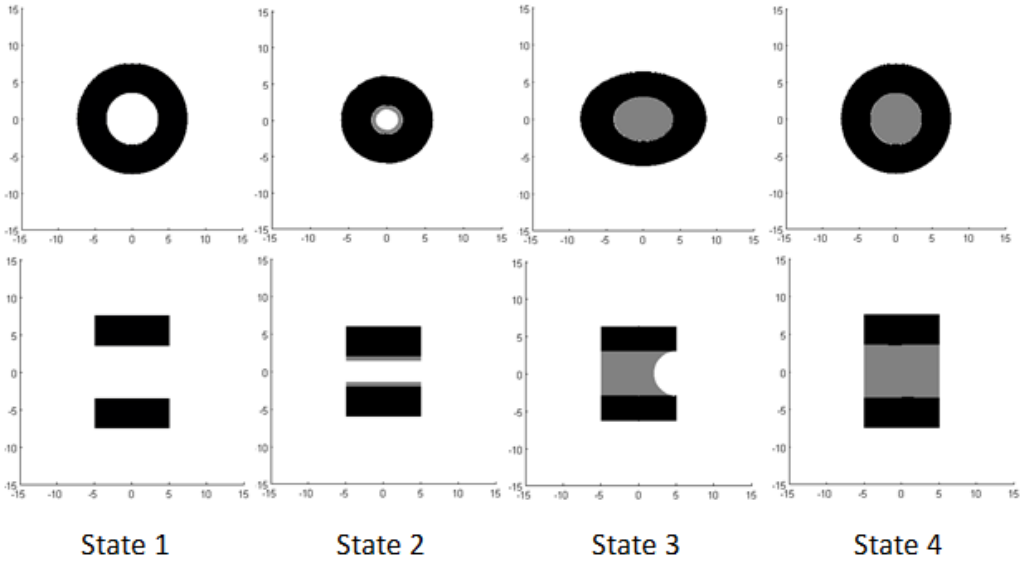

Figure 4.6 Model states that represent the four different configurations of MWNCTs and confined water in reference 13. The top row is a view of each model state along the tube axis, and the bottom row is a view of each model state in cross-section perpendicular to the tube axis. State 1 is an empty CNT with an inner diameter of 7 nm and outer diameter 15 nm. State 2 has a 1 nm thick cylindrical film of water and underwent a 20% uniform radial contraction. State 3 is a CNT with an elliptical cross-section and the contained water possesses an ellipsoidal meniscus with zero contact angle. State 4 is completely filled with water possessing flat menisci at each end, and the CNT has regained its original cross-section geometry. All of the axes are in nm[54].

The series of states modeled represent different instances along the progression of capillary condensation. The CNTs were modeled as 10 nm long tubule segments with electron densities taken as that of bulk material. The integrals over SAXS distributions corresponding to CNTs of constant cross section undergoing capillary condensation, and

CNTs of changing cross section without capillary condensation were also calculated. In chapter 2 it was stated in equation 2.17 that the SAXS distribution for a statistically homogeneous object is equal to the Fourier transform of the average electron density autocorrelation function. In calculating the SAXS distributions for the CNT model states the random orientation of the CNTs in the sample had to be accounted for. The scatter distribution for an object of random orientation is

$$I = \int \langle \mathcal{P}(\vec{x}) \rangle \, e^{-i\vec{q}\cdot\vec{x}} dv_x \qquad 4.1$$

where the angled brackets indicate averaging over rotational orientation.

The relations between the coordinates of points in an orthonormal right handed coordinate system rotated through the Eulerian angles relative to the coordinates of points in a fixed orthonormal right handed coordinate system were used in conjunction with a series of branching statements to generate the relevant electron density functions for each CNT model state,

$$\begin{aligned}
\xi_1 &= \xi_1'(cos\psi cos\varphi - sin\psi sin\varphi cos\theta) - \xi_3'(cos\psi sin\varphi + sin\psi cos\varphi cos\theta) \\
&\quad + \xi_2' sin\psi sin\theta \\
\xi_2 &= \xi_1'(sin\psi cos\varphi + cos\psi sin\varphi cos\theta) + \xi_3'(cos\psi cos\varphi cos\theta - sin\psi sin\varphi) \\
&\quad - \xi_2' cos\psi sin\theta \\
\xi_3 &= \xi_1' sin\varphi sin\theta + \xi_3' cos\varphi sin\theta + \xi_2' cos\theta
\end{aligned} \qquad 4.2$$

The i[th] coordinate of a point in the original un-rotated coordinate system ξ_i is a function of the three coordinates of the corresponding point in the rotated coordinate system, ξ_1', ξ_2', ξ_3', and the three Eulerian angles $\psi,\ \theta\ and\ \varphi$.[66] The angles $\psi,\ \theta\ and\ \varphi$ are the angles of

precession, nutation and pure rotation respectively. The above expressions were used to map the coordinates of each point of a rotated coordinate system whose orientation was specified by the three Euler angles back to the original un-rotated coordinate system. If the point in the rotated system corresponded to a point in the un-rotated system that resided within the volume of the assumed CNT model it was assigned the appropriate electron density. The CNT model tube axes was aligned along the third coordinate axis of the un-rotated coordinate system. For the model state with elliptical cross section (state 3) the logical criterion used to assign electron density values to each point in the rotated space was

$$\left(|\xi_3| \le \frac{h}{2}\right) \wedge \left(\left(\left[\left(\frac{\xi_1}{A}\right)^2 + \left(\frac{\xi_2}{B}\right)^2\right]^{-\frac{1}{2}} \le 1\right) \wedge \left(\left[\left(\frac{\xi_1}{a}\right)^2 + \left(\frac{\xi_2}{b}\right)^2\right]^{-\frac{1}{2}} \ge 1\right)\right)$$

$$\Leftrightarrow \rho(\xi_1', \xi_2', \xi_3') = \rho_{carbon}$$

$$\left(|\xi_3| \le \frac{h}{2}\right) \wedge \left(\left(\left[\left(\frac{\xi_1}{a}\right)^2 + \left(\frac{\xi_2}{b}\right)^2\right]^{-\frac{1}{2}} \le 1\right) \wedge \left(\left[\left(\frac{\xi_1}{a}\right)^2 + \left(\frac{\xi_2}{b}\right)^2 + \left(\frac{\xi_3 - \frac{h}{2}}{b}\right)^2\right] \ge 1\right)\right)$$

$$\Leftrightarrow \rho(\xi_1', \xi_2', \xi_3') = \rho_{water} \qquad 4.3$$

If both sentential forms had false truth values the point was assigned an electron density of zero. In the equations above A, B, a and b represent the semi-major and semi-minor axes of the outer and inner ellipses respectively that bound the distorted annular CNT cross section. The values of these axes were found by the implementation of an optimization algorithm with the circumference as the target function (Appendix 2). The perimeters of

the inner and outer ellipses were assumed equal to the circumferences of the inner and outer circles that bound the annular CNT cross section of the model state 2 representative of CNTs that underwent a uniform radial contraction after the formation of a thin liquid film. The constant electron densities ρ_{carbon} and ρ_{water} were calculated from bulk densities. The electron density ρ_{carbon} was adjusted accordingly for each model state such that the number of electrons was held constant as the cross section geometry changed.

In examining each point of a rotated space and assigning it an electron density essentially a summation of form factors weighted by the appropriate electron densities was being formed. For a given model the total electron density could be written

$$\rho(\vec{x}) = \rho_{carbon}\sigma_{carbon}(\vec{x}) + \rho_{water}\sigma_{water}(\vec{x}). \qquad 4.4$$

This expression demonstrates that the models used in the data interpretation satisfied the criterion of statistical homogeneity.

After evaluation of the sentential forms for each point of a rotated space the electron density function for a model state was specified. At this point the Fourier autocorrelation theorem was utilized to generate the autocorrelation function for the object space,

$$\mathcal{P}(\vec{x}) = \mathcal{F}^{-1}\{P^2\} \qquad 4.5$$

The electron density function for the model $\rho(\vec{x})$ was Fourier transformed to give $P(\vec{q})$, and the square of the modulus P^2 was calculated. The inverse Fourier transform of P^2, $\mathcal{F}^{-1}\{P^2\}$ is equal to the electron density autocorrelation function. This procedure for the generation of the electron density autocorrelation function was implemented for 500 distinct combinations of uniformly distributed Euler angles for a given CNT model state. The autocorrelation functions were then averaged, yielding $\langle\mathcal{P}\rangle$.

The object spaces used in these calculations had a box length of 127.5 nm and a linear point density of one point every 7.5 Å. The rotationally averaged autocorrelation function and therein the reciprocal space are spherically symmetric[47]. The spherical symmetry of the reciprocal space permits integration over a trace as opposed to the entire space. The lower limit of integration was taken as the minimum scatter angle to which our experimental geometry was sensitive, found by the procedure outline in section 3.4.

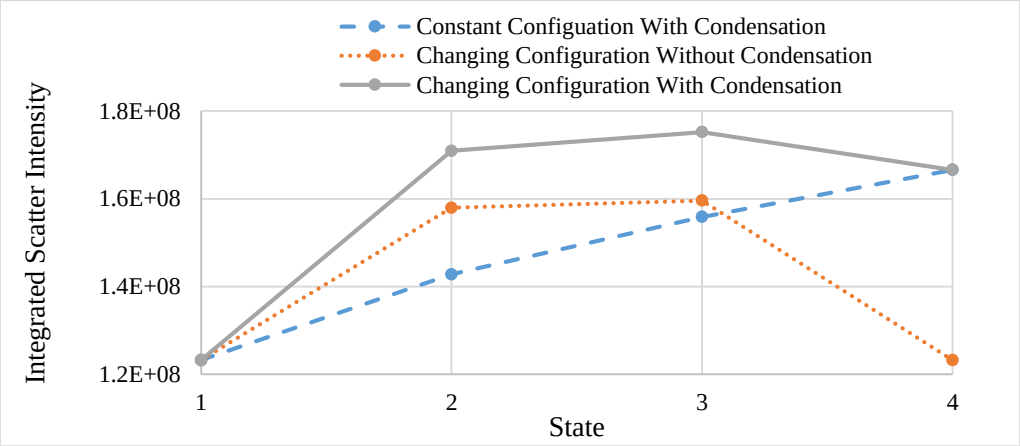

Figure 4.7 Numerical integration over SAXS distributions calculated for different CNT models by Simpson's method. The SAXS distributions were calculated using the procedure outlined in the text. The angular range of integration was [7.59×10^{-4} , 3.2×10^{-3}] radians. The progression of states from 1 to 4 correspond to capillary condensation. Only the series of models for changing CNT cross-section geometry and condensation produce a change in integrated scatter intensity that qualitatively agrees with the observed data for the as-purchased sample in Figure 4.5. The discrepancy between the other models used and the experimental data show that the integrated scatter signal is due to both the change in water content and the changing CNT cross-section geometry, and not to either attribute individually[54].

The proximity of the CNTs to each other was ignored in considering the shape of the SAXS distributions, or in other words it was assumed that the CNTs scatter

independently of each other. Independent scattering by the CNTs causes the SAXS distribution of a single CNT to have the same shape as that of the entire ensemble. The calculations were also carried out using the average wavelength of radiation emitted from the X-ray tube. The average wavelength was calculated to be 0.4 angstroms by taking a weighted average over the emission spectrum produced by the SpekCalc software package.

The CNT deformations used in the calculations were extrapolated from the changes in geometry observed by Rossi *et. al*.[13], who used CNTs with a patchwork wall structure. Therefore the model cross-section configurations used here are an upper limit to any deformation actually present in this experiment because CNTs of longer range order were used.

The calculated results of the integrated SAXS distributions for the model CNTs with changing cross-section and capillary filling shown in Figure 4.7 show qualitative agreement with the shape of the experimentally measured as-purchased integrated SAXS profile during condensation shown in Figure 4.5. The similarity between the theoretical and experimental data is taken as evidence that the CNTs and contained water in this study traverse the same sequence of states visited by those observed in reference 13 during capillary condensation. In Figure 4.7 the integrated scatter intensities for CNTs that change cross-section but do not undergo capillary condensation also exhibit a maximum but the scatter intensity returns to its initial value in state 4. This behavior is not observed experimentally during condensation, and the series of model states is not physically attainable. The integrated scatter intensities for the CNTs of constant cross-section that undergo capillary condensation show a monotonic increase in intensity. While a monotonic increase is observed in the condensation data for the functionalized sample (Figure 4.5)

this is due to a lack of control over the degree of filling resulting in incomplete capillary condensation, i.e. condensation stops at either state two or three in Figure 4.6. The differences between the calculated intensity profiles along the three different series of CNT cross-sections and degrees of filling indicate that the recorded scatter signal did not arise from either water content or CNT cross-section alone, but was the result of both the change in CNT cross-section and water content.

Unfortunately no agreement is found when the calculated integrated scatter intensities for the CNTs of changing configuration undergoing condensation are considered in reverse order, from state 4 to state 1, and are compared with any of the scatter profiles during evaporation. The discrepancy between the calculations and scatter intensities observed during evaporation reveal that the sequence of events taking place within the samples during evaporation is not simply the same set of events observed for condensation in reverse order.

As discussed in section 2.2 SAXS distributions are composed of at least two distinct regions, the Guinier and Porod. Figure 4.8 shows a log-log plot for one of the calculated SAXS distributions with the Porod region indicated by the appropriate straight line fit. The SAXS distribution used in the construction of this plot is the same as that presented in chapter 2. The shaded area in Figure 4.8 indicates spatial frequencies probed by the experiment. From Figure 4.8 it is easily seen that the experiment is only sensitive to changes within the Porod region of the distribution, implying that the change in scatter signal is more readily correlated to changes in the number and nature of interfaces within the sample than it is to changes in sample shape. The Porod region of a SAXS distribution is unaffected by the particle density of the sample, so the restriction of experimental

sensitivity to this region legitimizes the use of a SAXS distribution for a single CNT to be representative of the distribution for the entire sample to within a numerical constant.

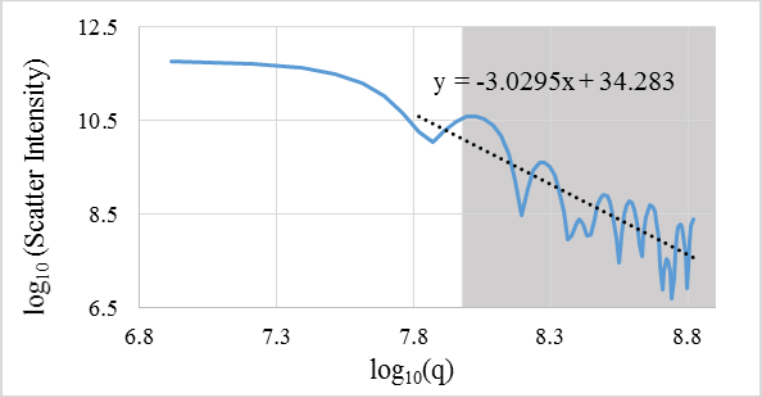

Figure 4.8 Log-Log plot of the a SAXS distribution for CNT model state 1 in Figure 4.6. The Porod region is indicated by the straight line fit whose equation is displayed. The Guinier region lies closer to the origin of reciprocal space. The shaded part of the plot covers the angular distribution probed by the imaging setup[54].

The linear fit to the Porod region of the SAXS distribution presented in Figure 4.8 has a slope of -3 as opposed to the previous claim that it should equal -4. The difference in asymptotic decay may be attributed to the discrete sampling of rotational orientations producing a fractal boundary surface for the rotationally averaged models[67].

The discrepancy between the integrated scatter profiles for evaporation and condensation could arise from a state visited by the CNTs during evaporation that is not visited during condensation, or bubbles could form during evaporation. Consider evaporation of water from the CNTs by starting at state 4 in Figure 4.6. The CNTs would be filled with water, and as water begins to evaporate the CNTs take on an elliptical cross section in state 3 causing an increase in scatter. If bubbles were to form on a time scale shorter than that of evaporation there would be an increase in the number of interfaces within the sample at constant mass. The generation of new interfaces would affect the

sample specific surface area and therein potentially produce a second increase in scatter similar to that observed in this study.

4.4.3 Change in Evaporation Time Scale with Temperature

The Kelvin equation was used to calculate the boiling point of 30 ^{o}C for water confined to the inner pore of CNTs used in this experiment. For the most accurate calculation equation 1.9 was not used. Instead the vapor pressure of the confined water was solved for in the Kelvin equation,

$$P = P_o e^{\frac{2v\gamma}{RTr}}, \qquad 4.6$$

as a function of temperature. It was assumed that water completely wets the inner surface of the CNTs. This seems to be a reasonable approximation since Barber et. al.[68] measured the contact angles of water on CNTs surfaces and found that the contact angle water makes with inner surface is less than that on the outer surface. Also the contact angle was slightly varied in the calculation of the boiling point and had a negligible effect. The change in CNT cross-section was ignored, so r in equation 4.6 is the inner radius of the MWCNTs, 3.5 nm.

Both the surface tension and the vapor pressure above a planar surface of water are functions of temperature, so equation 4.6 should be viewed as function of the temperature alone

$$P(T) = (T, P_0(T), \gamma(T)). \qquad 4.7$$

The vapor pressure of water above a planar surface as a function of temperature was calculated using the Antoine equation

$$log_{10}P_0 = A - \frac{B}{C+T}, \qquad 4.8$$

where A, B and C are empirical constants with values 6.20963, 2354.731 and 7.559 respectively[69]. The temperature dependent surface tension was calculated using the equation[70]

$$\gamma(T) = B\left(1 - \frac{T}{T_c}\right)^{\mu}\left[1 + b\left(1 - \frac{T}{T_c}\right)\right]. \qquad 4.9$$

The empirical constants B, μ and b have values 235.8x10^{-3} Nm^{-1}, 1.256 and -0.625 respectively. The critical temperature of water is denoted T_c and has the value 647.15 K.

The pressure inside of the glass vials containing the CNTs was assumed equal to that of water vapor pressure at 25 ^{o}C, so the temperature at which the vapor pressure above the meniscus was equal to the vapor pressure of water at 25 ^{o}C was taken as the boiling point for water confined by the CNTs, which was 30 ^{o}C. The predicted boiling point coincides with the change in evaporation time scales with temperature. The rate of evaporation decreases with decreasing temperature. More over the samples could be left for weeks at room temperature and evaporation from the CNTs would occur upon heating, and evaporation clearly occurs at 45 ^{o}C. Therefore, the boiling point for water confined to the inner pore of the CNTs is somewhere between room temperature and 45 ^{o}C. Experiments were not conducted at temperatures lower than 45 ^{o}C because the time it would take for evaporation to go to completion would far exceed 50 hours.

4.5 Conclusions

The similarity in scatter profiles for the functionalized and as-purchased samples during evaporation of water from the inner cavity of the CNTs indicates that functionalization of the CNT surfaces only affects the relative time scale of evaporation

and not the mechanism. Oxidation of the CNTs permitted permanent water adsorption onto the CNT surfaces at a temperature much higher than that observed for the as-purchased CNTs. Agreement between the calculated integrated scatter intensities and the observed shape of the integrated scatter profile during capillary condensation of the as-purchased sample indicates that the progression of CNT cross-section geometries and liquid volume configurations observed in reference 13 are the same as those in this experiment. Coincidence of the change in evaporation time scales with the boiling point predicted by the Kelvin equation and the qualitative agreement between the theoretical calculations and observed scatter intensity of the as-purchased sample during condensation establishes the applicability of equilibrium thermodynamics to water confined to dimensions less than 10 nm. To the author's knowledge this is the first experimental verification that equilibrium thermodynamics may be applied to liquids confined within this size regime, confirming the predictions by Thomas et. al.[24] The disparity between the theoretical calculations and scatter profiles recorded during evaporation reveal an absorption-desorption hysteresis. The hysteresis is thought to have its origin in either bubble formation or a CNT cross-section geometry not seen during capillary condensation.

Chapter 5 Electrochemical Reduction of CO_2 Using a Clathrate Hydrate Electrolyte

5.1 Clathrate Hydrate Electrolyte Preparation

Potassium bicarbonate of purity greater than 99.99% was purchased from Sigma-Aldrich and used to make a 0.1 M solution with nano-pure water. The purified water was generated using an 18.2 MΩ Milli-Q water purification system. An electrolysis was run for a minimum of 12 hours with continuous bubbling of Argon (Ar. 99.999%, Corp Brother) to ensure all trace amounts of metals were removed from the electrolyte. Tetrahydrofuran (T397 with 125 ppm BHT and T427SK with no BHT, Fisher Scientific) was added to the purified electrolyte solution such that it was 10% by mass THF. BHT stabilized THF was used due its increased safety profile and decreased concentration of reactive peroxides.

The electrolyte and THF solution was poured into a reactor that was mechanically stirred at 130 rpm and cooled to 274.5 K. The reactor was kept under a carbon dioxide atmosphere of 1.015 bar. The clathrates would form in 6 to 24 hours. A sample of the clathrate electrolyte solution was filtered in order to determine the %mass of the solution that formed clathrates. It was found that the electrolyte was 14% by mass clathrate crystallites. The clathrate electrolyte was found to contain 9 times the CO_2 concentration contained in the control solution, which possessed the same chemical composition but contained no crystallites.

Figure 5.1 Batch reactor constructed for the formation of the clathrate electrolyte solution. The inner chamber contains a helical Teflon structure used to continuously stir the electrolyte solution. The entire vessel is gas tight and placed under CO_2 pressure slightly above 1 atm. The reactor is also water jacketed for temperature control[71].

5.2 Electrochemical Reduction of CO_2

Electrolysis of the CO_2 loaded clathrate hydrate electrolyte solution was carried out in an H-type cell. The whole cell was gas tight, and the two compartments were separated by a Nafion proton-exchange membrane (Nafion 117, DuPont). The Nafion membrane was stored in electrolyte solution 12 hours prior to being used. The cell was placed in a circulating water bath to control temperature. Experiments using clathrates were conducted at 2.0 ^oC. Control experiments were conducted at 4.0 ^oC to prevent clathrate formation.

The H-type cell joint where the Nafion was placed was carefully wrapped in Parafilm to prevent contamination of the membrane. Prior to the application of a potential both chambers of the H-type cell were bubbled with CO_2 for 30 minutes at flow rate of approximately 20 ml/min.

A copper foam was used as the working electrode, and a custom-made Ag/AgCl electrode was used as a reference. The counter electrode was a platinum mesh. All potentials reported are reference to a Ag/AgCl electrode (+190 mV vs SHE). The copper foam electrodes were mechanically stable to the point that they maintained structural integrity during handling and the electrochemical experiments. A Pine Research Instrumentation AFCBP1 bipotentiostat was used to carry out the electrolysis experiments. Electrolysis was run at -1.0 V, -1.3 V and -1.7 V vs Ag/AgCl. Electrolysis at each voltage was repeated three times.

The reactivity of THF was determined by running electrolysis of the electrolyte solution that had not been exposed to a CO_2 stream. Only H_2 was produced confirming that THF was electrochemically inert under the experimental conditions used.

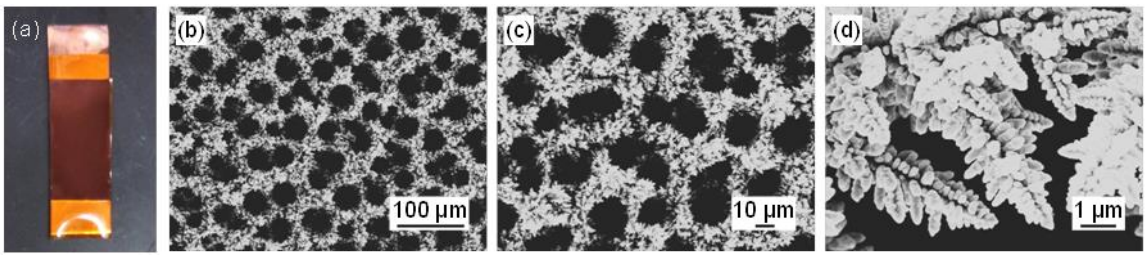

Figure 5.2 Picture of copper foam electrode. The dark brown band in the center of the electrode is foam **a**. The substrate is planar copper. Figures **b**, **c** and **d** are TEM images of the foam with increasing magnification[71].

5.3 Quantification of Products

5.3.1 Gaseous Products

One milliliter aliquots of the catholyte compartment headspace were injected into a Buck Scientific 910 gas chromatograph (GC). A GC spectrum was collected prior to injection of the sample to confirm the absence of contaminants. Gas product concentrations were averaged over aliquots from the three different experiments at each voltage. The Faradic efficiency (FE) of each gaseous product was calculated from the ratio of the measured product concentration to the concentration expected for 100% FE from the total charge passed during an electrolysis experiment. Faradic efficiency is reported as opposed to current efficiency because of the difficulty in determining the surface area of the copper foam electrode. The copper electrode has a honeycomb structure lined with dendritic protrusions.

5.3.2 Liquid Products

Aliquots of the clathrate electrolyte were taken from the catholyte compartment after each experiment and analyzed by 1D ^{1}H NMR. ^{1}H spectra were recorded on Bruker Avance DRX-400 (400 MHz) and Avance 600 (600 MHz) spectrometers. The THF and water peaks were suppressed by a modified version of the WET solvent suppression technique.

5.4 Results

Formic acid, H_2 and CO were found to be the major products produced while CH_4 and higher hydrocarbons were produced to a lesser degree. Figure 5.1 contains the Faradic efficiencies for the gaseous and liquid products for clathrate and non-clathrate electrolyte.

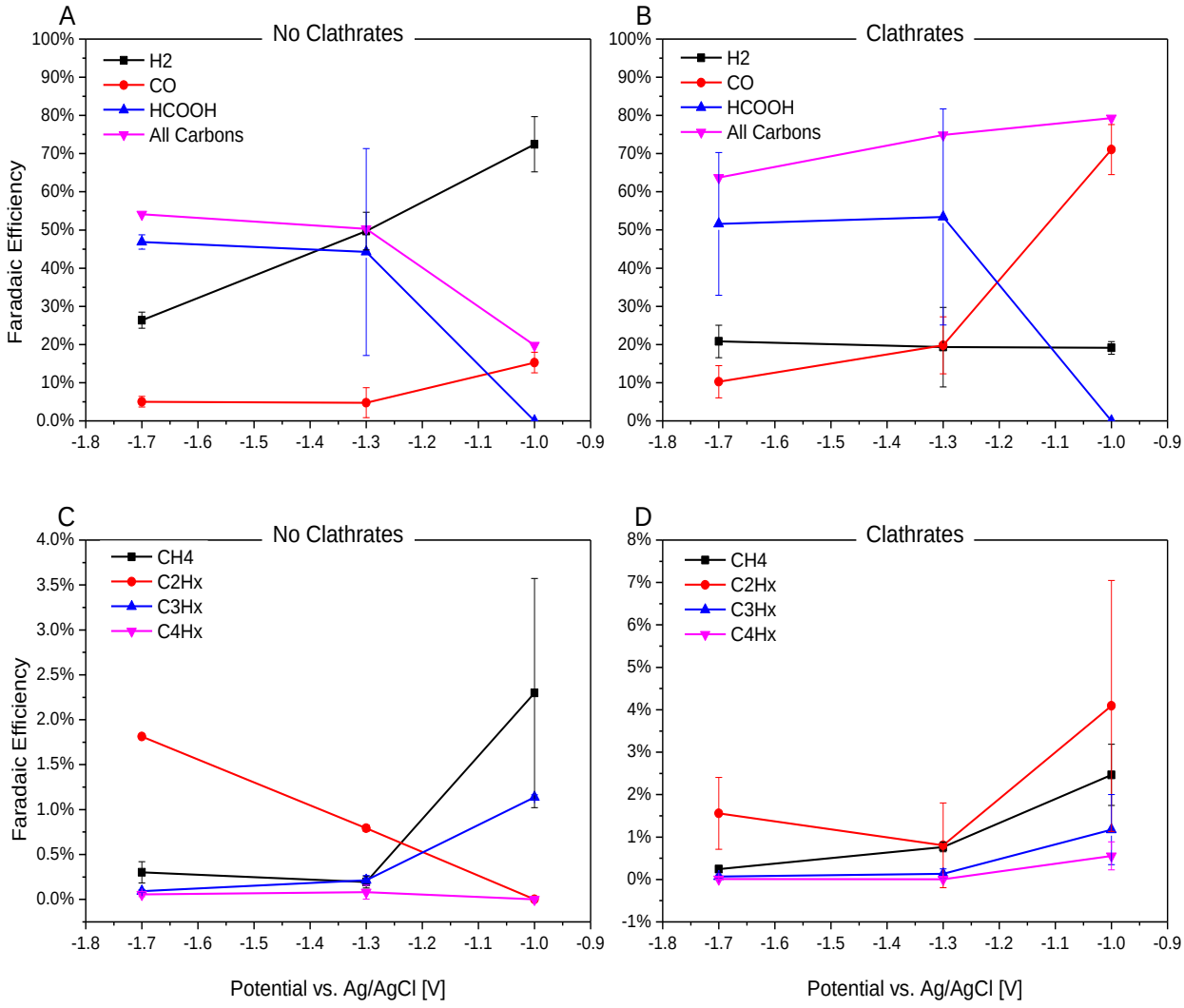

Figure 5.3 Faradic efficiency of gaseous and liquid products from the electrochemical reduction of CO_2. Figures **A** and **C** show the FE for products produced with an electrolyte devoid of clathrates, and Figures **B** and **D** show the FE for products produced with clathrate electrolyte[72].

The Faradic efficiencies in Figure 1 are scaled by a correction factor that accounts for the scavenging of radical protons by BHT. The scaling factor was determined by examining the suppression of the HER when TFH was used with and without BHT stabilizer. Figure 5.4 contains the relative FE for H_2 production with and without BHT present at -1.3 V and -1.0 V. Electrolysis was carried out for 20 minutes.

The small amount of BHT present in solution limits the probability of radical scavenging in the electrolytic double layer, especially at more reductive potentials, -1.7 V, where BHT is exhausted quickly. At more anodic potentials BHT should have a longer lasting effect. Based on BHT concentration it was predicted that BHT should be exhausted within 20-25 minutes at -1.3 V and 5 minutes at -1.7 V. These estimates were confirmed experimentally. During the first 20 minutes of electrolysis at -1.0 V or -1.3 V hydrogen production was significantly greater for the un-stabilized TFH solution compared to the stabilized. After 60 minutes the difference in hydrogen production between the stabilized and un-stabilized solutions decreased significantly. It seems that BHT in clathrate electrolytes affects HER but not the product distribution.

Hydrogen production is reduced in the presence of clathrates and the formation of carbon containing compounds is increased. The FE approached 100% at -1.0 V and -1.3 V. At -1.7 V the formation of liquid products could have been below the detection limit of NMR causing the decreased overall efficiency. Product formation at -1.7 V was nearly identical for the clathrate and control solutions. At -1.3 V the Faradic efficiencies of CO and CH_4 are higher when clathrates are present compared to when clathrates are absent. It cannot be determined if there is a change in the Faradaic efficiency of formic acid, and

there is no difference for C_2 products. At -1.0 V the Faradic efficiency of CO is 70% and that of gaseous hydrocarbons is 8% for the clathrate electrolyte compared to 15% and 3% for electrolyte without clathrates. The HER is suppressed to 20% at all potentials in the presence of clathrates permitting increased production of carbonaceous products.

5.5 Conclusion

It was demonstrated that the presence of clathrate hydrates significantly increases the Faradic efficiency for the production of carbonaceous products at low overpotentials while suppressing the HER. The production of heavier hydrocarbons was also promoted by the presence of clathrates. Movement of the CO_2 reduction product distribution toward more chemically valued species in the presence of clathrates is attributed to loading of the clathrate cages with CO_2 causing a substantial increase in CO_2 concentration within the electrolyte.

Appendix 1

X-ray Data with Error Bars

Below are Figures 4.4 and 4.5 from the text, but error bars for a 95% confidence interval are included.

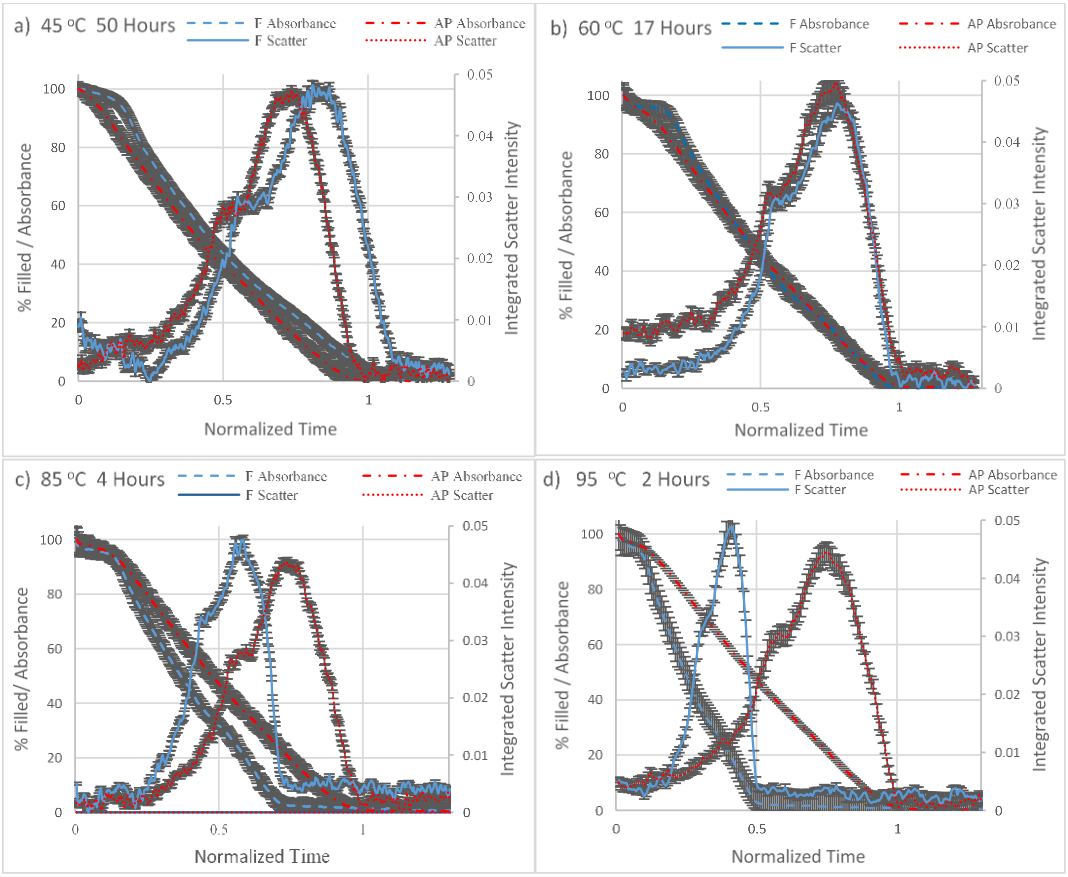

Figure A.4.4 Results of SFHI analysis on X-ray images of CNTs heated to different set point temperatures that were then maintained. The heat treated/functionalized sample is labeled as F, and the as-purchased sample is labeled AP. The left ordinate is rescaled absorbance values that represent the percent filling of the CNTs relative to the initial water content. The right ordinate is the integrated scatter intensity scale. The abscissa is time normalized to the when evaporation in the as-purchased sample went to completion. The time to which the abscissa was normalized is next to the set point temperature in each figure. The signals

shown are the differences of the signals from the wet samples and the signals from their corresponding dry samples. All signals have been offset corrected.

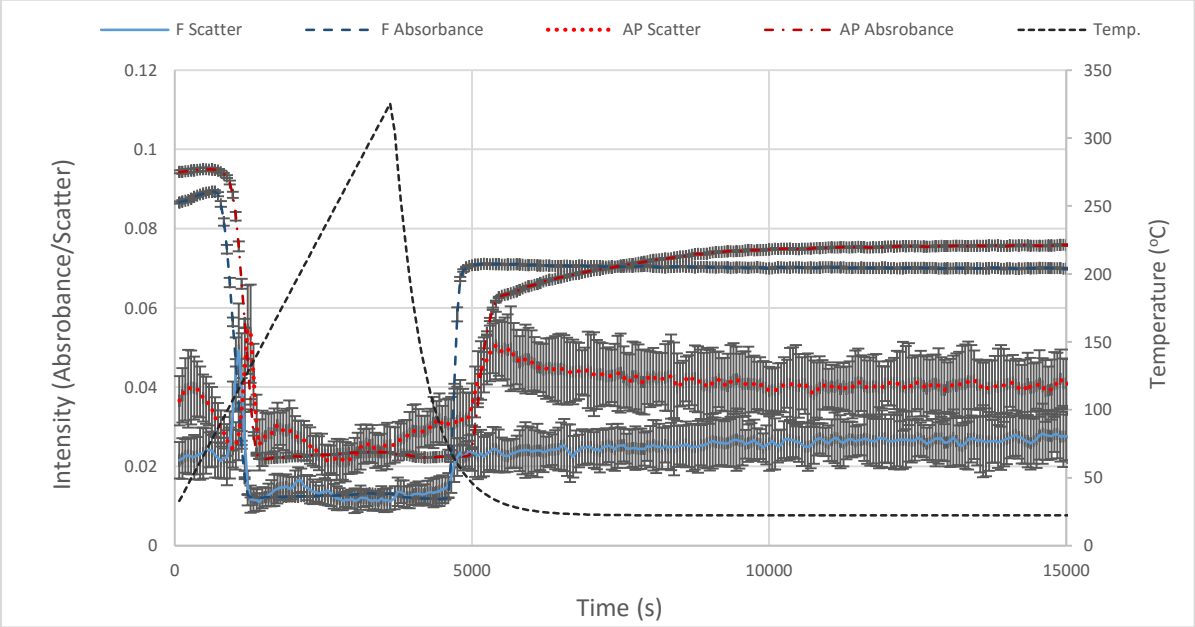

Figure A.4.5 Results of SFHI analysis on X-ray images of CNTs heated to 320 °C that were then permitted to cool by thermal radiation. The functionalized sample is labeled F and the as-purchased sample is labeled AP. The left ordinate is intensity for both absorbance and scatter and the right ordinate is a temperature scale. The signals shown are the differences between the samples containing water and their corresponding dry samples. All signals have been offset corrected.

Appendix 2

Optimization Algorithm for the Geometric Parameters of CNT Model State 3

The geometric parameters that define the different model states displayed in Figure 4.6 were extrapolated from the deformations of MWCNTs exposed to increasing water vapor pressure observed by Rossi et. al. It was assumed that in going from the circular cross-section geometry of the empty MWCNT a circular cross-section was produced by a 20% radial contraction upon the formation of a 1 nm thick water film on the inner surface of the CNT. After continued condensation once a lens shaped meniscus formed it was assumed that an elliptical MWCNT cross-section geometry was obtained where the circumference was maintained from the configuration about the thin film. To find the semi-major and semi-minor axes of the elliptical cross-section geometry an optimization algorithm was implemented.

First the semi-major and semi-minor axes, a and b, of the inner elliptical surface were found. In order to safeguard against arriving at a circular cross-section the values searched for a and b were confined to values 5 Å greater than and less than the circular radius respectively. The initial value of a was equal to the circular radius plus 5 Å. The initial value of b was 0 nm. Different axis values were tested in step sizes of 0.1 Å. Axis values that were considered to be permissible produced an ellipse with a perimeter that differed by no more than $\pm$ 0.1 Å from the circular cross-section circumference. The

perimeter of the ellipse was calculated by the complete elliptical integral of the second kind,

$$C = 4a \int_0^{\pi/2} \sqrt{1 - e^2 sin^2\theta}\, d\theta. \qquad \text{A.2.1}$$

The perimeter is C, e is the eccentricity

$$e = \sqrt{1 - \left(\frac{b}{a}\right)^2}, \qquad \text{A.2.2}$$

and θ is the polar angle. The integration was carried out using Simpson's method. Values of a and b were chosen from those satisfying the ascribed tolerance that produced the smallest change in elliptical perimeter from the circular circumference.

Once a and b were chosen the semi-major and semi-minor axes, A and B, of the outer elliptical surface were determined using almost identical reasoning. Again the perimeter of the outer elliptical surface was assumed equal to the outer circumference of the circular MWCNT cross-section. The values of A and B searched by the program were

$$R < A < 2R \quad \text{and} \quad (b + 0.01\ \text{Å}) < B < R. \qquad \text{A.2.3}$$

The outer radius of the circular cross-section is R. The values of A and B were then chosen from the set of values found to satisfy the same tolerance applied to the search for values of a and b. The specific values of A and B were those that produced the smallest difference in elliptical perimeter and the outer circular circumference of the contracted MWCNT.

Appendix 3

Design of Wave Mechanics Undergraduate Chemistry Laboratory

There is a paradoxical lack of an undergraduate laboratory focused on wave mechanics in chemistry curricula despite the necessity to introduce quantum principles in introductory chemistry classes. College freshmen have varied scientific backgrounds, so the only knowledge that can be assumed of them is what they are taught in their present course work. If this notion is taken as true chemistry students are exposed to the principles of quantum mechanics prior to having studied the physics of particles and waves. Introductory physics and engineering classes cover the nature of particles and waves, so by the time physics and engineering majors take quantum mechanics in later semesters these ideas are firmly in place. Chemistry is primarily concerned with the study of molecules, atoms and subatomic particles making an introduction to quantum mechanics necessary prior to any rigorous training in physics. A lecture oriented attempt aimed at filling in the missing physics would only turn a chemistry course into a highly condensed physics course, but a single laboratory intended to introduce basic wave mechanics and its relevance to quantum mechanics and chemistry through various demonstrations of resonance could only serve to increase understanding of wave phenomena without deviating from a pre-panned course outline. To this end an undergraduate laboratory was designed to increase the understanding of quantum principles introduced in lecture by better acquainting introductory chemistry students with wave mechanics through

observation of mechanical vibrations and surface plasmon resonance in silver nanoparticles.

The laboratory consists of two demonstrations of wave mechanics. The first demonstration provides a corporeal example through direct visualization of resonance phenomena by application of mechanical vibrations to bubble membranes. The second demonstration is made by carrying out the synthesis of silver nanoparticles and the observation of their surface plasmon frequencies by absorption spectroscopy. A series of pre and post laboratory questions attempt to establish a connection between classical resonance, the observations made during the laboratory and the solutions of Schrodinger's equation for a particle in a box.

The first demonstration of wave mechanics involves the mechanical vibration of bubble membranes in order to provide the students with direct visualization of wave phenomena. The students were asked to download a free frequency generator application on either their cell phones or computer. An 8 ohm speaker equipped with an amplification circuit was directly connect to the electronic device, and used to create mechanical vibrations of bubble membranes. By changing the frequency of vibration applied to the bubble membrane the students will directly observe that standing waves are only generated on the surface at specific frequencies and moreover that those frequencies change if the boundary conditions change.

Figure A.3.1 A circular boundary condition is shown in the image sitting on top of a speaker. A laptop with a frequency generator application is in the background.

The students then synthesize silver nanoparticles of different shapes and sizes and find their plasmon frequencies. The synthesis is as follows[73]: 25 mls of 0.1 mM silver nitrate, 1.5 ml of 30 mM trisodium citrate, 1.5 ml of 0.7 mM PVP and 0.4 mg of sodium borohydride.

$$Ag^{+}_{(aq)} + BH^{-}_{4\,(aq)} \xrightarrow[sodium\ citrate]{PVP} Ag_{(s)} + BH_3 + \frac{1}{2}H_2 \qquad \text{A.3.1}$$

This synthesis will produce silver nanospheres approximately 5 nm in diameter. By adding 60 ul of 30% hydrogen peroxide after the addition of sodium borohydride triangular prisms will be produced instead of spheres. The citrate and PVP act as surfactants that bind to the nucleated nanoparticles and keep them suspended in solution. The sodium borohydride reduces the ionic silver in solution to nucleate the nanoparticles and then continue their growth into spheres. The addition of hydrogen peroxide oxidizes neutral silver on the nanoparticles back into solution. Nanoparticles are small crystallites, and certain crystal faces are more reactive than others, so when the hydrogen peroxide oxidizes

silver back into solution the silver ions are then reduced again but bond on the more reactive crystal faces to yield triangular prisms.

The students then take an aliquot of the nanoparticle solutions and recorded the absorption spectra to identify their plasmon frequencies. The absorption spectrum of the spherical particles contains a single plasmon frequency as there is a single geometric parameter that specifies its shape. The spectrum for the prisms contains multiple peaks corresponding to the multiple geometric parameters that are needed to specify its shape.

Plasmon frequencies can be described using quantum mechanics, but even if the students are given the relevant equations they are complicated, typically involving special functions. Freshmen cannot be expected to deal with such mathematics when their primary computing sources are hand held calculators and excel. Also plasmon frequencies can be addressed using classical electrodynamics. This is why this part of the lab is presented as an additional demonstration of classical wave mechanics at the mesoscale and not as quantum mechanics.

The students were then given a series of post laboratory questions that were meant to guide them in making connections between their observation of standing waves produced by mechanical vibration, the interpretation of nanoparticle absorption spectra in terms of resonances for different boundary conditions (nanoparticle size and shape) and the interpretation of the wave function for a quantum particle in a box as a standing wave. This line of reasoning, and other relevant supplementary arguments provided in the laboratory manual, permitted further questioning about basic quantum topics typically discussed in introductory chemistry lectures, i.g. the de Broglie wavelength, Heisenberg uncertainty and the interpretation of the wave function as a probability density.

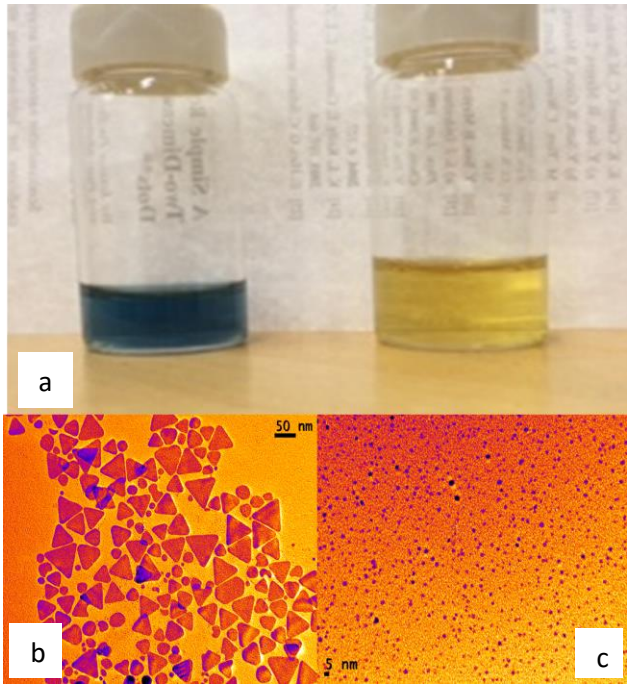

Figure A.3.2 Aliquots of the nanoprisms (blue) and nanospheres (yellow) **a**. TEM images of the nanoprisms **b** and nanospheres **c**.

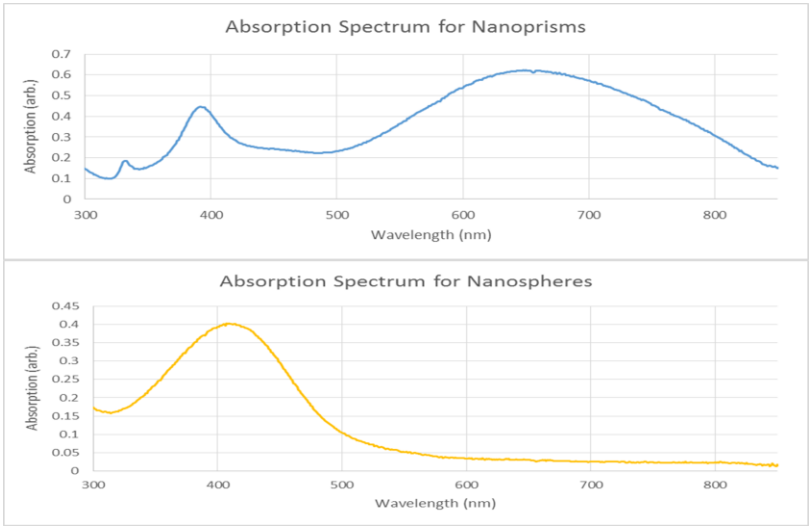

Figure A.3.3 Absorption spectra for the nanoprisms and spheres. The prisms have multiple resonance frequencies corresponding to the different geometric parameters, and the spheres only have one resonance.

The laboratory served as the makeup lab in the Fall of 2015 for students that missed a regularly scheduled laboratory earlier in the semester. Fourteen students participated in the lab. They worked in pairs to minimize the number of speaker assemblies that had to be produced. The analytical balances were not leveled prior to the start of the laboratory. The mass of the sodium borohydride used was within the error of the balances so a number of different sized nanoparticles were produced by the students. The particles produced were probably formed a size and shape spectrum with small spherical nanoparticles (red solution) at one end and large prisms (purple solution) at the other shown in Figure A.3.3. As long as the two solutions made by a given pair of students possessed different colors the laboratory report could still be completed because the nanoparticles would have at least a shift in the plasmon resonance if not also a change in the number of resonances.

Figure A.3.4 Nanoparticle solutions produced by students during the execution of the laboratory. The analytical balances were not leveled prior to the experiment so the small mass of reducing agent required for the synthesis was inaccurately measured and produced a variety of nanoparticles as seen by their different plasmon resonances.

List of Published Works and Those Still in Progress

Published

- Schunk, F. M.; Rand, D.; Rose-Petruck, C., Spatial Frequency Heterodyne Imaging of Aqueous Phase Transitions inside Multi-walled Carbon Nanotubes. *PCCP* **2015,** *17,* 31237-31246
- DeCiccio, D.; Ahn, S. T.; Sen, S.; Schunk, F. M.; Palmore, G. T. R.; Rose-Petruck, C., Electrochemical reduction of CO_2 with clathrate hydrate electrolytes and copper foam electrodes. *Electrochem. Comm.* **2015,** *52,* 13-16.

In Progress

- The undergraduate laboratory presented in Appendix 3 will be submitted to the Journal of Chemical Education
- SFHI of Clathrate Hydrate formation and loading of CO_2
- SFHI of nanoparticle synthesis from molecular salts, and conversion between different types of nanoparticles

References

1. Gardeniers, H., Chemistry in nanochannel confinement. *Anal. Bioanal. Chem.* **2009,** *394*.

2. Gelb, L. D.; Gubbins, K. E.; Radhakrishnan, R.; Sliwinska-Bartkowiak, M., Phase separation in confined systems. *Reports on Progress in Physics* **1999,** *62*, 1573-1659.

3. Heuberger, M.; Zach, M.; Spencer, N. D., Density Fluctuations Under Confinement: When is a Fluid Not a Fluid? *Science* **2001,** *292* (5518), 905-908.

4. Mattia, D.; Gogotsi, Y., Review: static and dynamic behavior of liquids inside carbon nanotubes. *Microfluidics and Nanofluidics* **2008,** *5*, 289-305.

5. Di Ventra, M.; Evoy, S.; Heflin, J. R., *Introduction to Nanoscale Science and Technology*. Springer: New York, NY, 2004.

6. Guggenheim, E. A., *Thermodynamics*. Elsevier: New York, NY, 1967.

7. Butt, H.; Graf, K.; Kappl, M., *Physics and Chemsitry of Interfaces*. Wiley: Federal Republic of Germany, 2003.

8. Sui, H.; Han, B.; Lee, J. K.; Walian, P.; Jap, B. K., Structural basis of water-specific transport though the AQP1 water channel. *Nature* **2001,** *414*, 872-878.

9. Chialvo, A. A.; Vlcek, L.; Cole, D. R., Aqueous CO2 Solutions at Silica Surfaces and within Nanopore Environments. Insights from Isobaric-Isothermal Molecular Dynamics. *Journal of Physical Chemistry C* **2012,** *116*, 13904-13916.

10. Singhal, R.; Mochalin, V. N.; Lukatskaya, M. R.; Friedman, G.; Gogotsi, Y., Separation and liquid chromatography using a single carbon nanotube. *Scientific Reports* **2012,** *2* (510), 1-6.

11. Fornasiero, F.; Park, H. G.; Holt, J. K.; Stadermann, M.; Grigopoulos, C. P.; Noy, A.; Bakajin, O., Ion exclusion by sub-2-nm carbon nanotube pores. *PNAS* **2008,** *105* (45), 17250-17255.

12. Dujardin, E.; Ebbesen, T. W.; Hiura, H.; Tanigaki, K., Capillarity and Wetting of Carbon Nanotubes. *Science* **1994,** *265* (5180), 1850-1852.

13. Rossi, M. P.; Gogotsi, Y.; Kornev, K. G., Deformation of Carbon Nantubes by Exposure to Water Vapor. *Langmuir* **2009,** *25*, 2804-2810.

14. de Gennes, P.; Brochard-Wyart, F.; Quere, D., *Capillarity and Wetting Phenomena*. Springer: New York, NY, 2004.

15. Everett, D. H.; Haynes, J. M., Model Studies of Capillary Condensation. *J. Colloid Interface Sci.* **1972,** *38*, 125-137.

16. Yazicioglu, A. G.; Megaridis, C. M.; Nicholls, A.; Gogotsi, Y., Electron Microscope Visualization of Multiphase Fluids Contained in Closed Carbon Nanotubes. *Journal of Visualization* **2005,** *8* (2), 137-144.

17. Maniwa, Y.; Kataura, H.; Abe, M.; Suzuki, S.; Achiba, Y.; Kira, H.; Matsuda, K., Phase Transition in confined Water Inside Carbon Nanotubes. *Journal of the Physical Society of Japan* **2002,** *71* (12), 2863-2866.

18. Kyakuno, H.; Matsuda, K.; Yahiro, H.; Inami, Y.; Fukuoka, T.; Miyata, T.; Yanagi, K.; Kataura, H.; Saito, T.; Yumura, M.; Ijima, S., Confined water inside single-walled

carbon nanotubes: Global phase diagram and effect of finite length. *Journal of Chemical Physics* **2011,** *134*, 244501-244514.

19. Maniwa, Y.; Kataura, H.; Masatoshi, A.; Udaka, A.; Suzuki, S.; Achiba, Y.; Kira, H.; Matsuda, K.; Kadowaki, H.; Okabe, Y., Ordered water inside carbon nanotubes: formation of pentagonal to octagonal ice-nanotubes. *Chem. Phys. Lett.* **2005,** *401*, 534-538.

20. Wang, H.; Xi, X.; Kleinhammes, A.; Wu, Y., Temperature-Induced Hydrophobic-Hydrophilic Transition Observed by Water Adsorption. *Science* **2008,** *322*, 80-83.

21. Kolesnikov, A. I.; Zanotti, J.; Loong, C.; Thiyagarajan, P., Anomalously Soft Dynamics of Water in a Nanotube: A Revelation of Nanoscale Confinement. *Phys. Rev. Lett.* **2004,** *93* (3), 035503-1 - 035503-4.

22. Liu, Y.; Wang, Q.; Wu, T.; Zhang, L., Fluid structure and transport properties of water inside carbon nanotubes. *J. Chem. Phys.* **2005,** *123* (234701), 1-7.

23. Sadeghi, M.; Parsafar, G. A., Density-induced molecular arrangements of water inside carbon nanotubes. *PCCP* **2013,** *15*, 7379-7388.

24. Thomas, J. A.; McGaughey, A. J. H., Density, distribution, and orientation of water molecules inside and outside carbon nanotubes. *J. Chem. Phys.* **2008,** *128* (084715), 1-6.

25. Hori, Y.; Kikuchi, K.; Suzuki, S., Production of CO and CH_4 in electrochemical reduction of CO_2 at metal electrodes in aqueous hydrogencarbonate solution. *Chem. Lett.* **1985,** *14*, 1695-1698.

26. Carroll, J. J.; Slupsky, J. D.; Mather, A. E., The solubility of carbon dioxide in water at low pressure. *J. Phys. Chem. Ref. Data* **1991,** *20*, 1201-1209.

27. Hara, K.; Kudo, A.; Sakata, T., Electrochemical reduction of carbon dioxide under high pressure on various electrodes in an aqueous electrolyte. *J. Electroanal. Chem.* **1995,** *391*, 141-147.

28. Sloan, E. D.; Koh, C. A., *Clathrate Hydrates of Natural Gases Third Ed.* CRC Press: Boca Raton, FL, 2008.

29. Seo, Y. T.; Moudrakovski, J. A.; Ripmeester, J. A.; Lee, J. W.; Lee, H., Efficient recovery of CO_2 from flue gas by clathrate hydrate formation in porous silica gels. *Environ. Sci. Technol.* **2005,** *39*, 2315-2319.

30. Clark, M. A.; Bishnoi, P. R., Determination of the intrinsic kinetics of CO_2 gas hydrate formation using in situ particle size analysis. *Chem. Eng. Sci.* **2005,** *60*, 695-709.

31. Dholabhai, P. D.; Kalogerakis, N.; Bishnoi, P. R., Equilibrium conditions for carbon dioxide hydrate formation in aqueous electrolyte solutions. *J. Chem. Eng. Data* **2002,** *38*, 650-654.

32. Anderson, G. K., Enthalpy of dissociation and hydration numer of carbon dioxide hydrate from the Clapeyron equation. *J. Chem. Thermodyn.* **2003,** *35*, 1171-1183.

33. Duan, Z.; Sun, R., A model to predict phase equilibrium of CH_4 and CO_2 clathrate hydrate in aqueous electrolyte solutions. *Am. Mineral* **2006,** *91*, 1346-1354.

34. Circone, S.; Kirby, S. H.; Stern, L. A., Thermodynamic calculations in the system CH_4-H_2O and methane hydrate phase equilibria. *J. Phys. Chem. B* **2006,** *110*, 8232-8239.

35. Kiyono, F., Separation and recovery of CO_2 from exhausted gas by hydrates. *Prepr. Symp. Am. Chem. Soc. Div. Fuel Chem.* **2000,** *45*, 671-675.

36. Mohammadi, A. H.; Anderson, R.; Tohidi, B., Carbon monoxide clathrate hydrates: equilibrium data and thermodynamic modeling. *AIChE J.* **2005,** *51*, 2825-2833.

37. Davidson, D. W.; Desando, M. A.; Gough, S. R.; P., H. Y.; Ratcliffe, C. I.; Ripmeester, J. A.; Tse, J. S., A clathrate hydrate of carbon monoxide. *Nature (London)* **1987,** *328*, 418-419.

38. Mao, W. L.; Mao, H. K.; Goncharov, A. F.; Struzhkin, V. V.; Guo, Q. Z.; Hu, J. Z.; Shu, J. F.; Hemley, M.; Somayazulu, Y. S.; Zhao, Y. S., Hydrogen clusters in clathrate hydrate. *Science* **2002,** *297*, 2247-2249.

39. Cady, G. H., Composition of clathrate gas hydrates of H_2S, Xe, SO_2, Cl_2, CH_3Cl, CH_3Br, $CHClF_2$, CCl_2F_2, and C_3H_8. *J. Phys. Chem.* **1983,** *87*, 4437-4441.

40. Kumar, R.; Linga, P.; Moudrakovski, I.; Ripmeester, J. A.; Englezos, P., Structure and kinetics of gas hydrates from methane/ethane/propane mixtures relevant to the design of natural gas hydrate storate and tansport facilities. *AIChE J.* **2008,** *54*, 2132-2144.

41. Linga, P.; Kumar, R.; Englezos, P., Gas hydrate formation from hydrogen/carbon dioxide and nitrogen/carbon dioxide gas mixtures. *Chem. Eng. Sci.* **2007,** *62*, 4268.

42. Linga, P.; Kumar, R.; Englezos, P., Capture of carbon dioxide from conventional power plants or from integrated gasification plants through gas hydrate formation/dissociation. *J. Energy Clim. Chang.* **2006,** *1*, 75.

43. Linga, P.; Kumar, R.; Ripmeester, J. A.; Englezos, P., *Hydrate processes for CO_2 capture and scale up using a new apparatus*. ICGH: British Columbia, Vancouver, 2008.

44. Linga, P.; Adeyemo, A.; Englezos, P., Medium-pressure clathrate hydrate/membrane hybrid process for postcombustion caputre of carbon dioxide. *Environ. Sci. Technol.* **2007,** *42*, 315-320.

45. Kang, S. P.; Lee, H., Recovery of CO_2 from flue gas using gas hydrate: thermodynamic verification through phase equilibrium measurements. *Environ. Sci. Technol.* **2000,** *34*, 4397.

46. Guinier, A., *X-ray Diffraction In Crystals, Imperfect Crystals, and Amorphous Bodies*. Dover: New York, NY, 1994.

47. Wrinch, D., *Fourier Transforms and Structure Factors*. The American Society for X-ray and Electron Diffraction: 1946.

48. Wen, H.; Bennett, E. E.; Hegedus, M. M.; Carroll, S. C., Spatial Harmonic Imaging of X-ray Scattering -- Initial Results. *IEEE Transactions on Medical Imaging* **2008,** *27* (8), 997-1002.

49. Stein, A. F.; Ilavsky, J.; Kopace, R.; Bennett, E. E.; Wen, H., Selective imaging of nano-particle contrast agents by a signle-sho x-ray diffraction technique. *Optics Express* **2010,** *18* (12), 13271-13278.

50. Wen, H.; Bennett, E. E.; Hegedus, M. M.; Rapacchi, S., Fourier X-ray Scattering Radiography Yields Bone Structural Information. *Radiology* **2009,** *251* (3), 910-918.

51. Wu, B.; Liu, Y.; Rose-Petruck, C.; Diebold, G. J., X-ray Spatial frequency heterodyne imaging. *Applied Physics Letters* **2012,** *100*, 061110.

52. Liu, Y.; Ahr, B.; Linkin, A.; Diebold, G. J.; Rose-Petruck, C., X-ray spatial harmonic imaging of phase objects. *Optics Letters* **2011,** *36* (12), 2209-2211.

53. Rand, D.; Ortiz, V.; Liu, Y.; Derdak, Z.; Wands, J. R.; Taticek, M.; Rose-Petruck, C., Nanomaterials for X-ray Imaging: Gold Nanoparticle Enhancement of X-ray Scatter Imaging of Hepatocellular Carcinoma. *Nano Letters* **2011,** *11*, 2678-2683.

54. Schunk, F. M.; Rand, D.; Rose-Petruck, C., Spatial Frequency Heterodyne Imaging of Aqueous Phase Transitions inside Multi-walled Carbon Nanotubes. *PCCP* **2015,** *17*, 31237-31246.

55. Rand, D. X-Ray Spatial Frequency Heterodyne Imaging of Hepatocellular Carcinoma Using Nanoparticle Contrast Agents. Brown, Providence, RI, 2014.

56. Poludniowski, G. G.; Evans, P. M., Calculation of x-ray spectra emerging from an x-ray tube. Part I. Electron penetration characteristics in x-ray targets *Med. Phys.* **2007,** *34*, 2164.

57. Poludniowski, G. G., Calculation of x-ray spectra emerging from an x-ray tube. Part II. X-ray production and filtration in x-ray targets *Med. Phys.* **2007,** *34*, 2164.

58. Poludniowski, G. G.; Landry, G.; Delois, F.; Evans, P. M.; Verhaegen, F., SpekCalc: a program to calculate photon spectra from tungsten anode x-ray tubes. *Phys. Med. Biol.* **2009,** *54*, 19.

59. Li, W. Z.; Wen, J. G.; Ren, Z. F., Effect of temperature on growth and structure of carbon nanotubes by chemical vapr deposition. *Applied Physics A* **2002,** *74*, 397-402.

60. Ugarte, D.; Stockli, T.; Bonard, J. M.; Chatelain, A.; Heer, W. A. d., Filling Carbon Nanotubes. *Applied Physics A* **1998,** *67*, 101-105.

61. Ugarte, D.; Chatelain, A.; Heer, W. A. d., Nanocapillarity and Chemistry in Carbon Nanotubes. *Science* **1996,** *274*, 1897-1899.

62. Tasis, D.; Tagmatarchis, N.; Bianco, A.; Prato, M., Chemistry of Carbon Nanotubes. *Chem. Rev.* **2006,** *106*, 1105-1136.

63. Ebbesen, T. W.; Takada, T., Topological and SP^3 Defect Structures in Nanotubes. *Carbon* **1995,** *33* (7), 973-978.

64. Haddon, R. C., Chemistry of the Fullerenes: The Manifestation of Strain in a Class of Continuous Aromatic Molecules. *Science* **1993,** *261*, 1545-1550.

65. Ebbesen, T. W., Carbon Nanotubes. *Physics Today* **1996**, 26-32.

66. Boriskenko, A. I.; Tarapov, I. E., *Vector and Tensor Analysis with Applications*. Prentice-Hall Inc.: 1968.

67. Bale, H. D.; Schmidt, P. W., Small-Angle X-ray-Scattering Investigation of Submicroscopic Porosity with Fractal Properties. *Phys. Rev. Lett.* **1984,** *53* (6), 596-599.

68. Barbar, A. H.; Cohen, S. R.; Wagner, H. D., External and internal wetting of carbon nanotubes with organic liquids. *Phys. Rev. Lett. B* **2005,** *71* (115443), 1-5.

69. Gubkov, A. N.; Fermor, N. A.; Smirnov, N. I., Vapor Pressure of Mono-Poly Systems. *Zh. Prikl. Khim (Leningrad)* **1964,** *37*, 2204-2210.

70. Vargaftik, N. B.; Volkov, B. N.; Voljak, L. D., International Tables of the Surface Tension of Water. *J. Phys. Chem. Ref. Data* **1983,** *12* (3), 817-820.

71. DeCiccio, D. Electrochemical Reduction of Carbon Dioxide using Clathrate Hydrates. Brown, Providence, RI, 2015.

72. DeCiccio, D.; Ahn, S. T.; Sen, S.; Schunk, F. M.; Palmore, G. T. R.; Rose-Petruck, C., Electrochemical reduction of CO_2 with clathrate hydrate electrolytes and copper foam electrodes. *Electrochem. Comm.* **2015,** *52*, 13-16.

73. Metraux, G. S.; Mirkin, C. A., Rapid Thermal Synthesis of Silver Nanoprisms with Chemically Tailorable Thickness. *Adv. Mater.* **2015,** *17* (4), 412-415.